Polygonal Eyewalls, Asymmetric Eye Contraction, and Potential Vorticity Mixing in Hurricanes

WAYNE H. SCHUBERT, MICHAEL T. MONTGOMERY, RICHARD K. TAFT, THOMAS A. GUINN,*
SCOTT R. FULTON,+ JAMES P. KOSSIN, AND JAMES P. EDWARDS

Department of Atmospheric Science, Colorado State University, Fort Collins, Colorado

(Manuscript received 19 June 1997, in final form 25 February 1998)

ABSTRACT

Hurricane eyewalls are often observed to be nearly circular structures, but they are occasionally observed to take on distinctly polygonal shapes. The shapes range from triangles to hexagons and, while they are often incomplete, straight line segments can be identified. Other observations implicate the existence of intense mesovortices within or near the eye region. Is there a relation between polygonal eyewalls and hurricane mesovortices? Are these phenomena just curiosities of the hurricane's inner-core circulation, or are they snapshots of an intrinsic mixing process within or near the eye that serves to determine the circulation and thermal structure of the eye?

As a first step toward understanding the asymmetric vorticity dynamics of the hurricane's eye and eyewall region, these issues are examined within the framework of an unforced barotropic nondivergent model. Polygonal eyewalls are shown to form as a result of barotropic instability near the radius of maximum winds. After reviewing linear theory, simulations with a high-resolution pseudospectral numerical model are presented to follow the instabilities into their nonlinear regime. When the instabilities grow to finite amplitude, the vorticity of the eyewall region pools into discrete areas, creating the appearance of polygonal eyewalls. The circulations associated with these pools of vorticity suggest a connection to hurricane mesovortices. At later times the vorticity is ultimately rearranged into a nearly monopolar circular vortex. While the evolution of the finescale vorticity field is sensitive to the initial condition, the macroscopic end-states are found to be similar. In fact, the gross characteristics of the numerically simulated end-states are predicted analytically using a generalization of the minimum enstrophy hypothesis. In an effort to remove some of the weaknesses of the minimum enstrophy approach, a maximum entropy argument developed previously for rectilinear shear flows is extended to the vortex problem, and end-state solutions in the limiting case of tertiary mixing are obtained.

Implications of these ideas for real hurricanes are discussed.

1. Introduction

For fully three-dimensional nonhydrostatic motions with diabatic and frictional effects, the Rossby–Ertel potential vorticity (PV) equation based on dry potential temperature is

$$\frac{D}{Dt}(\alpha\boldsymbol{\zeta}\cdot\boldsymbol{\nabla}\theta) = \alpha\boldsymbol{\zeta}\cdot\boldsymbol{\nabla}\dot{\theta} + \alpha(\boldsymbol{\nabla}\times\mathbf{F})\cdot\boldsymbol{\nabla}\theta, \quad (1.1)$$

where D/Dt is the material derivative, α the specific volume, $\boldsymbol{\zeta} = 2\boldsymbol{\Omega} + \boldsymbol{\nabla}\times\mathbf{u}$ the absolute vorticity vector, $\mathbf{u}$ the three-dimensional velocity vector, θ the potential temperature, $\dot{\theta}$ the diabatic heating rate, and $\mathbf{F}$ the frictional force per unit mass (for a succinct review of PV ideas and their relevance to tropical cyclone dynamics, see (McIntyre 1993). In a hurricane, the potential vorticity $\alpha\boldsymbol{\zeta}\cdot\boldsymbol{\nabla}\theta$ is not materially conserved because of the diabatic and frictional terms on the right-hand side of (1.1). The diabatic term is particularly important and can be written as $\alpha|\boldsymbol{\zeta}|\mathbf{k}\cdot\boldsymbol{\nabla}\dot{\theta}$, where $\mathbf{k} = \boldsymbol{\zeta}/|\boldsymbol{\zeta}|$ is a unit vector pointing along the vorticity vector and $\mathbf{k}\cdot\boldsymbol{\nabla}\dot{\theta}$ is the derivative of diabatic heating along this unit vector. In the intense convective region of a hurricane the absolute vorticity vector tends to point upward and radially outward. Since $\dot{\theta}$ tends to be a maximum at midtropospheric levels, air parcels flowing inward at low levels and spiraling upward in the convective eyewall experience a material increase in PV due to the $\alpha\boldsymbol{\zeta}\cdot\boldsymbol{\nabla}\dot{\theta}$ term. This material increase of PV can be especially rapid in lower-tropospheric regions near the eyewall, where both $\alpha|\boldsymbol{\zeta}|$ and $\mathbf{k}\cdot\boldsymbol{\nabla}\dot{\theta}$ are large. Although the $\alpha\boldsymbol{\zeta}\cdot\boldsymbol{\nabla}\dot{\theta}$ term reverses sign at upper-tropospheric levels, large PV is

* Current affiliation: USAF, Hickam AFB, Hawaii.
+ Permanent affiliation: Department of Mathematics and Computer Science, Clarkson University, Potsdam, New York.

Corresponding author address: Dr. Wayne H. Schubert, Department of Atmospheric Science, Colorado State University, Fort Collins, CO 80523-1371.
E-mail: waynes@hadley.atmos.colostate.edu

often found there because the large lower-tropospheric values of PV are carried upward into the upper troposphere. The resulting spatial structure of the PV field might be expected to be a tower of high PV. Although this conceptual model seems reasonably accurate, it needs some refinement related to the eye region. Once an eye has formed, there is no latent heat release in the central region, and large values of PV would not tend to occur there unless they were transported in from the eyewall. The resulting spatial structure of the PV field might then be expected to be a tower of high PV with a hole in the center or, equivalently, an annular tower of high PV with low PV in the central region. We shall refer to such a structure as a hollow tower of PV. This structure is nicely illustrated in the idealized axisymmetric model results of Möller and Smith (1994). The reversal of the radial PV gradient near the eyewall might also be expected to set the stage for dynamic instability (Montgomery and Shapiro 1995) and rearrangement of the PV distribution. If, during the rearrangement process, part of the low PV fluid in the eye is mixed into the eyewall, asymmetric eye contraction can occur in conjunction with a polygonal eyewall. While PV maps of hurricanes are beginning to be constructed from various types of available data (Shapiro and Franklin 1995; Shapiro 1996), we still need much more observational evidence for the finescale PV mixing that is likely occurring continuously in the inner core of hurricanes. A tantalizing aspect of the polygonal eyewall phenomenon is that it may be a small window on such PV mixing.

The two most complete observational studies of polygonal eyewalls are those of Lewis and Hawkins (1982) and Muramatsu (1986). Lewis and Hawkins examined polygonal eyewalls using time-lapse plan position indicator (PPI) film recordings of storms observed by land-based radars (Hurricanes David 1979; Anita 1977; Caroline 1975; Betsy 1965) and by airborne radars (Hurricanes Debbie 1969; Anita 1977). Their photographic analyses revealed that hurricane eyes can be in the shapes of hexagons, pentagons, squares, and triangles. Although the polygons were frequently incomplete, the straight line configurations were easily discernible. Lewis and Hawkins also noted that, while circular and elliptical eyes were also observed in the film recordings, they were seldom present for very long before straight lines and angles would appear. In addition, by showing that individual patterns could be simultaneously observed with two different radar systems, they disproved the possibility that polygonal shapes are artifacts of a particular radar system. Finally, Lewis and Hawkins also argued that polygonal eyes were not caused by topographic features near land-based radars, since polygonal features were also observed from airborne radars hundreds of kilometers from land.

At present, the most detailed radar observations of polygonal eyes have been obtained from Typhoon Wynne 1980, when it passed Japan's Miyakojima radar (Muramatsu 1986). Observations from this small, remote island consisted of 15 h of PPI images showing polygonal eye features. During this period Wynne's central surface pressure was between 920 and 935 mb. The polygonal features varied between square, pentagonal, and hexagonal, all of which rotated counterclockwise around the center. The pentagonal (which occurred most frequently) and hexagonal shapes had rotational periods of approximately 42 min, while the square shape had a rotational period of approximately 48 min. In addition, by presenting other radar and satellite images, Muramatsu offered further evidence that polygonal eyewalls are indeed real phenomena. Combining his observations with those of Lewis and Hawkins, Muramatsu defined some common characteristics of hurricanes exhibiting polygonal eyewalls. His results indicated that polygonal eyewalls were present in well-developed hurricanes having concentric eyewalls. Central pressures ranged from 920 to 950 mb, square to hexagonal eyewalls were most frequent, and the polygonal patterns tended to persist for tens of minutes. Contrary to Lewis and Hawkins, Muramatsu found no evidence of triangular patterns.

Lewis and Hawkins' explanation for the existence of polygonal eyewalls was based largely on the internal gravity wave theories for spiral bands presented by Willoughby (1978) and Kurihara (1976). The basic idea is that gravity wave interference patterns due to the superposition of differing wavenumbers and periods would tend to produce polygonal bands. However, the existence of spiral bands can be explained without the use of transient gravity waves, but rather with PV dynamics and vortex Rossby waves (Guinn and Schubert 1993; Montgomery and Kallenbach 1997). According to these PV arguments, the inner spiral bands of hurricanes can form during the merger or axisymmetrization of asymmetric PV anomalies initiated internally by moist convection or externally through environmental forcing. It should also be mentioned that sharp bends in spiral bands, such as observed by Lewis and Hawkins for the case of Hurricane Caroline (1975), were observed in the numerical integrations of Guinn and Schubert (1993) whenever an existing vortex merged with another region of relatively high PV. In the present paper we shall explore the possibility that polygonal eyewalls can also be explained using PV dynamics.

Although Muramatsu (1986) did not develop a formal dynamical theory for the formation of polygonal eyes, he did suggest the phenomenon was related to an instability in the large shears of tangential wind near the inner edge of the eyewall (barotropic instability). Of special significance was the connection Muramatsu made between the formation of polygonal eyewalls and the formation of tornado suction vortices (Fujita et al. 1972). Although the two phenomena involve different scales, Muramatsu conjectured that both are related to barotropic instability. The barotropic instability of hurricane-scale annular PV rings was first explored by Guinn (1992) using a shallow water model.

With the exception of the recent work by Guinn

(1992), the study of polygonal eyewalls has been given little attention since their discovery, perhaps for two reasons. First, some researchers simply do not believe polygonal features actually exist; they believe such ''apparent features'' are due to peculiarities in particular radar observing systems. Second, though they accept their existence, many researchers view polygonal eyewalls as a curiosity having little bearing on fundamental scientific questions such as hurricane motion, structure, and intensity change. Here we shall argue that polygonal eyes are more than just a curiosity and are of interest because they are symptoms of finescale PV mixing processes that are occurring continuously near the center of a hurricane.

Questions regarding the development of large horizontal shears, the possible barotropic instability of hurricane flows, and the formation of eyewall mesovortices are also of critical importance for the safe operation of reconnaissance aircraft and for the prediction of surface wind damage in landfalling storms (Wakimoto and Black 1994; Willoughby and Black 1996). Black and Marks (1991) have presented NOAA/P3 aircraft data from the eyewall region of Hurricane Hugo (1989) showing horizontal wind shears of 60 m s^{-1} over less than 1 km. They have also shown that such large horizontal shears can be associated with mesovortices having strong signatures in the vertical motion and radar reflectivity fields. More recently, Hasler et al. (1997) have used 1-min *GOES-9* images and concurrent NOAA/P3 radar observations to confirm the existence of an eyewall mesovortex in Hurricane Luis (1995). The mesovortex in Luis was apparently associated with hurricane track oscillations that could be interpreted as a series of eight cycloidal loops.

The outline of the present paper is as follows. In section 2 we argue, through use of linear stability analysis, that polygonal eyewalls can form simply as a result of barotropic instability. Although somewhat new to tropical cyclones, this idea has been used previously to examine the related subject of tornado suction vortices (e.g., Snow 1978; Staley and Gall 1979, 1984; Rotunno 1982, 1984; Gall 1982, 1983; Steffens 1988; Lin 1992; Finley 1997). Direct numerical simulations with the fully nonlinear equations, interpreted in terms of vorticity dynamics, are presented in sections 3 and 4 in support of our hypothesis. The method adopted here involves numerical simulations with the simplest model—an unforced barotropic nondivergent model. We demonstrate that the evolution of the PV field bears a striking resemblance to both radar and satellite images of eyewall features. However, since our simple model is not capable of predicting clouds and the observational data in hurricanes is not yet of sufficient quality and quantity to produce fine grain (Rossby–Ertel) PV maps, the connection between the evolution of PV fields and the evolution of convective fields is indirect but suggestive. Analytical predictions of the ultimate end-state of the mixing process based on minimum enstrophy and maximum entropy arguments are presented in sections 5 and 6, respectively. Section 7 concludes with a brief discussion of the relevance of the ideas developed here to real hurricanes.

2. Linear stability analysis of an annular region of vorticity

In a mature hurricane the frictional stress varies quadratically with wind speed and consequently the vertical velocity at the top of the boundary layer tends to be maximized just inside the radius of maximum tangential wind (Eliassen and Lystad 1977). Neglecting asymmetric processes, the frictionally forced vertical velocity organizes the convection into an annular ring near the radius of maximum winds. The cyclonic shear zone on the inner edge of the eyewall convection can be envisaged as an annular ring of uniformly high PV, with large radial PV gradients on its edges. On the inner edge of the annular ring the PV increases with radius, while on the outer edge the PV decreases with radius. In terms of PV (Rossby) wave theory, a PV wave on the inner edge of the annular ring will propagate counterclockwise relative to the flow there, while a PV wave on the outer edge will propagate clockwise relative to the flow there. Thus, it is possible for these two counterpropagating (relative to the tangential flow in their vicinity) PV waves to have the same angular velocity relative to the earth, that is, to be phase locked. If the locked phase is favorable, each PV wave will make the other grow, and exponential instability will result. This barotropic idealization is one view of the origin of polygonal eyewalls. In reality baroclinic and diabatic effects must also be important (after all, the basic-state PV field results from diabatic effects), but here we shall isolate the barotropic processes in order to investigate the extent to which they explain polygonal eyewall features.

Consider a circular basic-state vortex whose tangential wind $\overline{v}(r)$ is a given function of radius r. Using cylindrical coordinates (r, ϕ), assume that the small-amplitude perturbations of the streamfunction, $\psi'(r, \phi, t)$, are governed by the linearized barotropic nondivergent vorticity (Rossby wave) equation

$$\left(\frac{\partial}{\partial t} + \overline{\omega}\frac{\partial}{\partial \phi}\right)\nabla^2\psi' - \frac{\partial \psi'}{r\partial \phi}\frac{d\overline{\zeta}}{dr} = 0, \qquad (2.1)$$

where $\overline{\omega}(r) = \overline{v}(r)/r$ is the basic-state angular velocity, $\overline{\zeta}(r) = d(r\overline{v})/rdr$ the basic-state relative vorticity, $(u', v') = (-\partial\psi'/r\partial\phi, \partial\psi'/\partial r)$ the perturbation radial and tangential components of velocity, and $\partial(rv')/r\partial r - \partial u'/r\partial\phi = \nabla^2\psi'$ the perturbation vorticity.[1] Searching

[1] Throughout this paper the symbols u, v are used to denote radial and tangential components of velocity when working in cylindrical coordinates and eastward and northward components of velocity when working in Cartesian coordinates.

for modal solutions of the form $\psi'(r, \phi, t) = \hat{\psi}(r)e^{i(m\phi - \nu t)}$, where m is the tangential wavenumber and ν the complex frequency, we obtain from (2.1) the radial structure equation

$$(\nu - m\overline{\omega})\left[r\frac{d}{dr}\left(r\frac{d\hat{\psi}}{dr}\right) - m^2\hat{\psi}\right] + mr\frac{d\overline{\zeta}}{dr}\hat{\psi} = 0. \quad (2.2)$$

A useful stability model of an annular region of vorticity that admits analytical solution is the piecewise constant model studied by Michalke and Timme (1967), Vladimirov and Tarasov (1980), and Dritschel (1989). For the basic-state tangential wind defined by

$$r\overline{v}(r) = \frac{1}{2}\begin{cases}\xi_1 r^2 + \xi_2 r^2 & 0 \le r \le r_1,\\ \xi_1 r_1^2 + \xi_2 r^2 & r_1 \le r \le r_2,\\ \xi_1 r_1^2 + \xi_2 r_2^2 & r_2 \le r < \infty,\end{cases} \quad (2.3)$$

the corresponding basic-state relative vorticity is

$$\overline{\zeta}(r) = \frac{\partial(r\overline{v})}{r\partial r} = \begin{cases}\xi_1 + \xi_2 & 0 < r < r_1,\\ \xi_2 & r_1 < r < r_2,\\ 0 & r_2 < r < \infty,\end{cases} \quad (2.4)$$

where ξ_1, ξ_2, r_1, and r_2 are constants. The constants ξ_1 and ξ_2 are the vorticity jumps (as one moves inward) at r_1 and r_2. The case in which we are most interested has $\xi_1 < 0$ and $\xi_2 > 0$, that is, a ring of elevated vorticity.

Restricting study to the class of perturbations whose disturbance vorticity arises solely through radial displacement of the basic-state vorticity, then the perturbation vorticity vanishes everywhere except near the edges of the PV ring, that is, (2.1) reduces to $\nabla^2\psi' = 0$ for $r \neq r_1$ and $r \neq r_2$, or equivalently, (2.2) reduces to

$$r\frac{d}{dr}\left(r\frac{d\hat{\psi}}{dr}\right) - m^2\hat{\psi} = 0 \quad \text{for } r \neq r_1, r_2. \quad (2.5)$$

The general solution of (2.5) in the three regions separated by the radii r_1 and r_2 can be constructed from different linear combinations of r^m and r^{-m} in each region. This approach results in six undetermined constants. Requiring boundedness of $\hat{\psi}(r)$ as $r \to 0$ and $r \to \infty$, and requiring continuity of $\hat{\psi}(r)$ at $r = r_1$ and $r = r_2$, reduces the number of undetermined constants to two [see section 4b of Michalke and Timme (1967) for details]. An alternative and more physically revealing approach is to write the general solution of (2.5), valid in any of the three regions, as a linear combination of the basis functions $B_1^{(m)}(r)$ and $B_2^{(m)}(r)$, defined by

$$B_1^{(m)}(r) = \begin{cases}(r/r_1)^m & 0 \le r \le r_1,\\ (r_1/r)^m & r_1 \le r < \infty,\end{cases} \quad (2.6a)$$

$$B_2^{(m)}(r) = \begin{cases}(r/r_2)^m & 0 \le r \le r_2,\\ (r_2/r)^m & r_2 \le r < \infty.\end{cases} \quad (2.6b)$$

The solution for $\hat{\psi}(r)$ is then

$$\hat{\psi}(r) = \Psi_1 B_1^{(m)}(r) + \Psi_2 B_2^{(m)}(r), \quad (2.7)$$

where Ψ_1 and Ψ_2 are complex constants. Since $dB_1^{(m)}/dr$ is discontinuous at $r = r_1$, the solution associated with the constant Ψ_1 has vorticity anomalies concentrated at $r = r_1$ and the corresponding streamfunction decays away from $r = r_1$. Similarly, since $dB_2^{(m)}/dr$ is discontinuous at $r = r_2$, the solution associated with Ψ_2 has vorticity anomalies concentrated at $r = r_2$ and the corresponding streamfunction decays away from $r = r_2$.

To relate Ψ_1 and Ψ_2, let us now integrate (2.2) over the narrow radial intervals between $r_1 - \epsilon$ and $r_1 + \epsilon$ and between $r_2 - \epsilon$ and $r_2 + \epsilon$ to obtain the jump (pressure continuity) conditions

$$\lim_{\epsilon\to 0}\left\{(\nu - m\overline{\omega}_1)r_1\left[\frac{d\hat{\psi}}{dr}\right]_{r_1-\epsilon}^{r_1+\epsilon}\right\} = \xi_1 m\hat{\psi}(r_1), \quad (2.8a)$$

$$\lim_{\epsilon\to 0}\left\{(\nu - m\overline{\omega}_2)r_2\left[\frac{d\hat{\psi}}{dr}\right]_{r_2-\epsilon}^{r_2+\epsilon}\right\} = \xi_2 m\hat{\psi}(r_2), \quad (2.8b)$$

where $\overline{\omega}_1 = \overline{\omega}(r_1)$ and $\overline{\omega}_2 = \overline{\omega}(r_2)$, and where we have assumed $\nu \neq m\overline{\omega}_1$ and $\nu \neq m\overline{\omega}_2$. Substituting the solution (2.7) into the jump conditions (2.8) yields the matrix eigenvalue problem

$$\begin{pmatrix} m\overline{\omega}_1 - \frac{1}{2}\xi_1 & -\frac{1}{2}\xi_1(r_1/r_2)^m \\ -\frac{1}{2}\xi_2(r_1/r_2)^m & m\overline{\omega}_2 - \frac{1}{2}\xi_2\end{pmatrix}\begin{pmatrix}\Psi_1\\ \Psi_2\end{pmatrix} = \nu\begin{pmatrix}\Psi_1\\ \Psi_2\end{pmatrix}. \quad (2.9)$$

The eigenvalues of (2.9) are given by

$$\nu = \frac{1}{2}(\nu_1 + \nu_2) \pm \frac{1}{2}[(\nu_1 - \nu_2)^2 + \xi_1\xi_2(r_1/r_2)^{2m}]^{1/2}, \quad (2.10)$$

where $\nu_1 = m\overline{\omega}_1 - \frac{1}{2}\xi_1$ and $\nu_2 = m\overline{\omega}_2 - \frac{1}{2}\xi_2$ are the pure (noninteracting) discrete vortex Rossby wave frequencies at the inner and outer interfaces. One can verify from (2.10) that ν must be real for $m = 1, 2$. This implies the vorticity field will remain stable to these disturbance patterns. The remaining wavenumbers can, however, produce frequencies with nonzero imaginary parts.[2]

If the basic-state vorticity jump at the outer interface were removed, the lower-left matrix element in (2.9) would disappear and the vortex Rossby wave on the inner interface would propagate with angular velocity ν_1/m. Similarly, if the basic-state vorticity jump at the inner interface were removed, the upper-right matrix element in (2.9) would disappear and the vortex Rossby wave on the outer interface would propagate with angular velocity ν_2/m. Thus, the system (2.9) can be re-

[2] In the analogous problem possessing a continuous basic-state vorticity profile, a) $m = 2$ can become exponentially unstable and b) an algebraic continuous-spectrum instability for $m = 1$ also exists and becomes nonlinear at large times even if the profile supports no exponential instabilities for $m = 2, 3, \ldots$ (Smith and Rosenbluth 1990). Whether a similar algebraic instability exists in the piecewise constant model when sheared disturbances are allowed is an interesting, unresolved question.

garded as a concise mathematical description of the interaction of two discrete counterpropagating vortex Rossby waves. The upper-right matrix element in (2.9) gives the effect of the outer vorticity anomaly pattern on the behavior of the inner interface, while the lower-left matrix element in (2.9) gives the effect of the inner vorticity anomaly pattern on the behavior of the outer interface. Note that the effect of these interactions decays with increasing wavenumber and decreasing values of the ratio r_1/r_2. For $\xi_1 < 0$ and $\xi_2 > 0$, the inner PV wave propagates counterclockwise relative to the basic-state tangential flow at $r = r_1$, while the outer PV wave propagates clockwise relative to the basic-state tangential flow at $r = r_2$.

To more easily interpret the eigenvalue relation (2.10), it is convenient to minimize the number of adjustable parameters. To write (2.10) in a different form we first define the average vorticity over the region $0 \le r \le r_2$ as $\zeta_{av} = \xi_1\delta^2 + \xi_2$, where $\delta = r_1/r_2$. Then, defining $\gamma = (\xi_1 + \xi_2)/\zeta_{av}$ as the ratio of the inner-region vorticity to the average vorticity, we can express ξ_1 and ξ_2 in terms of ζ_{av}, δ,γ as $\xi_1 = -\zeta_{av}(1 - \gamma)/(1 - \delta^2)$ and $\xi_2 = \zeta_{av}(1 - \gamma\delta^2)/(1 - \delta^2)$. Using these last two relations, and noting that $\overline{\omega}_1 = \frac{1}{2}\gamma\zeta_{av}$ and $\overline{\omega}_2 = \frac{1}{2}\zeta_{av}$ we can rewrite (2.10) as

$$\frac{\nu}{\zeta_{av}} = \frac{1}{4}\Bigg\{m + (m-1)\gamma \pm \Bigg[\left(m - (m-1)\gamma - 2\left(\frac{1-\gamma\delta^2}{1-\delta^2}\right)\right)^2 + 4\left(\frac{1-\gamma\delta^2}{1-\delta^2}\right)\left(\gamma - \frac{1-\gamma\delta^2}{1-\delta^2}\right)\delta^{2m}\Bigg]^{1/2}\Bigg\}. \tag{2.11}$$

Using (2.11) we can calculate the dimensionless complex frequency ν/ζ_{av} as a function of the disturbance tangential wavenumber m and the two basic-state flow parameters δ and γ. The imaginary part of ν/ζ_{av}, denoted by ν_i/ζ_{av}, is a dimensionless measure of the growth rate. Isolines of ν_i/ζ_{av} as a function of δ and γ for $m = 3, 4, \ldots, 8$ are shown in Fig. 1. Note that all basic states with $\gamma < 1$ satisfy the Rayleigh necessary condition for instability but that most of the region $\gamma < 1$, $\delta < ½$ is in fact stable. Clearly, thinner annular regions (larger values of r_1/r_2) should produce the highest growth rates but at much higher tangential wavenumbers. Note also the overlap in the unstable regions of the γ–δ plane for different tangential wavenumbers. For example, the lower right area of the γ–δ plane is unstable to all the tangential wavenumbers $m = 3, 4, \ldots, 8$. We can collapse the six panels in Fig. 1 into a single diagram if, for each point in the γ–δ plane, we choose the largest growth rate of the six wavenumbers $m = 3, 4, \ldots, 8$. This results in Fig. 2, which shows clearly the preference for higher wavenumbers as the annular ring becomes thinner.

Excluding values of δ larger than 0.9, the lower-right quarter of Fig. 2 contains isolines of the dimensionless growth rate ν_i/ζ_{av} between approximately 0.1 and 1.0, so that the dimensional growth rate ν_i satisfies $0.1\zeta_{av} \le \nu_i \le \zeta_{av}$. The average vorticity inside r_2 can be expressed as the circulation around r_2 ($2\pi r_2 v_2$) divided by the area inside r_2 (πr_2^2), that is, $\zeta_{av} = 2v_2/r_2$. For a strong hurricane we can choose $v_2 = 50$ m s^{-1} at $r_2 = 50$ km, in which case $\zeta_{av} = 2 \times 10^{-3}$ s^{-1}. Then we have $2.0 \times 10^{-4} \le \nu_i \le 2.0 \times 10^{-3}$ s^{-1}, or in terms of the *e*-folding time $\tau_e = \nu_i^{-1}$, $8.3 \le \tau_e \le 83$ min. Although consideration of tangential wavenumbers larger than 8 and values of δ larger than 0.9 will yield even faster growth rates, such rapid growth rates are probably not realistic since they require very thin vorticity rings. However, basic-state structures yielding instabilities with 8–80 min *e*-folding times may be relevant to understanding hurricane structure.

3. Pseudospectral barotropic nondivergent model

Given a sign reversal in the radial PV gradient at lower-tropospheric levels in the hurricane, one expects the stage to be set for a convectively modified version of combined barotropic–baroclinic instability and PV redistribution. Since the PV field in the hurricane is induced by both boundary layer and moist processes, we generally expect these same processes, along with barotropic and baroclinic instability effects, to play a role in the evolution of asymmetric disturbances developing out of this background state. Regardless of the importance of boundary layer and moist processes, it is instructive to understand the conservative dynamics before nonconservative processes are included. With this viewpoint in mind we examine first the conservative (weakly dissipative) nonlinear vorticity dynamics using an unforced barotropic nondivergent model. Future work will investigate the implications of these preliminary results in a divergent barotropic and three-dimensional setting with and without nonconservative processes.

Insight into the early time nonlinear evolution of an annular vortex has been obtained by Dritschel (1986) and Lin (1992) using the method of contour dynamics/contour surgery (Zabusky et al. 1979; Zabusky and Overman 1983; Dritschel 1988, 1989; Ritchie and Holland 1993). This method is specifically designed for piecewise-constant vorticity distributions such as the one used in the three region model of section 2. In short, the method predicts the position of the contours separating the regions of constant vorticity. An initially unstable annulus of uniform vorticity with small undulations on its inner and outer contours can distort and evolve into a pattern in which the vorticity becomes ''pooled'' into rotating elliptical regions connected to each other by filaments or strands of high vorticity fluid. As the filaments become more and more intricately stretched and folded, contour dynamics/contour surgery adds more nodes to accurately follow the elongating contours, but also surgically removes finescale features. Surgical removal of vorticity during the simulation of

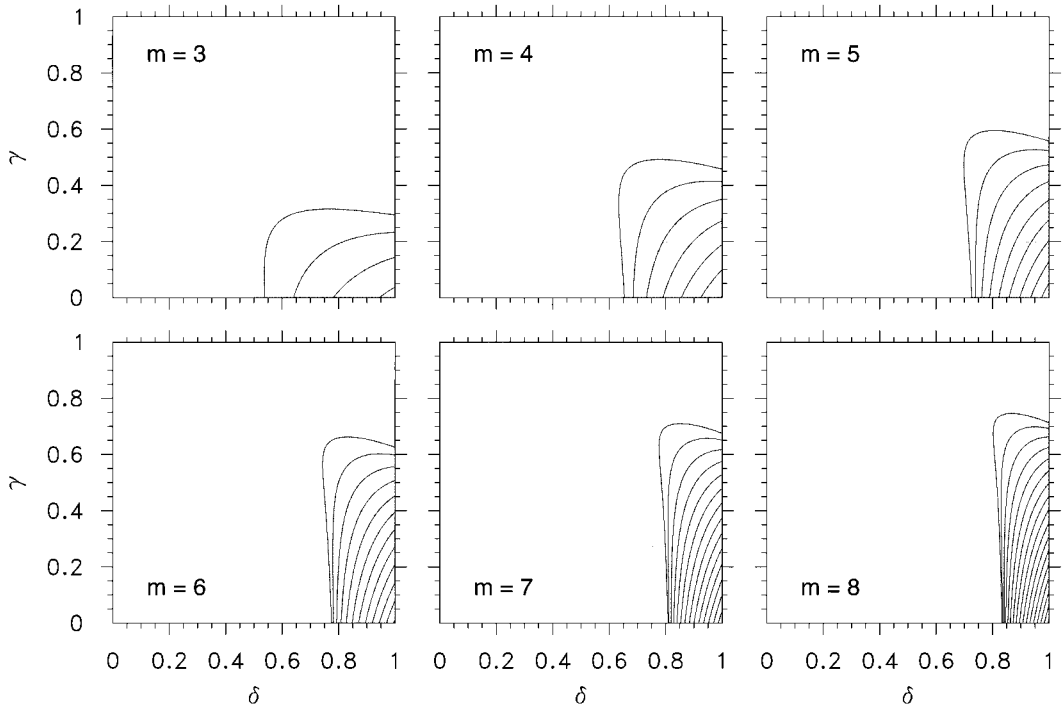

FIG. 1. Isolines of the dimensionless growth rate ν_i/ζ_{av}, computed from Eq. (2.11), as a function of δ and γ for tangential wavenumbers $m = 3, 4, \ldots, 8$. The parameter γ is the ratio of the inner region basic-state vorticity to the average basic-state vorticity inside r_2. Positive growth rates occur only in the shaded regions. The displayed isolines are $\nu_i/\zeta_{av} = 0.1, 0.2, 0.3, \ldots$ with the largest growth rates occurring in the lower-right corner of each figure.

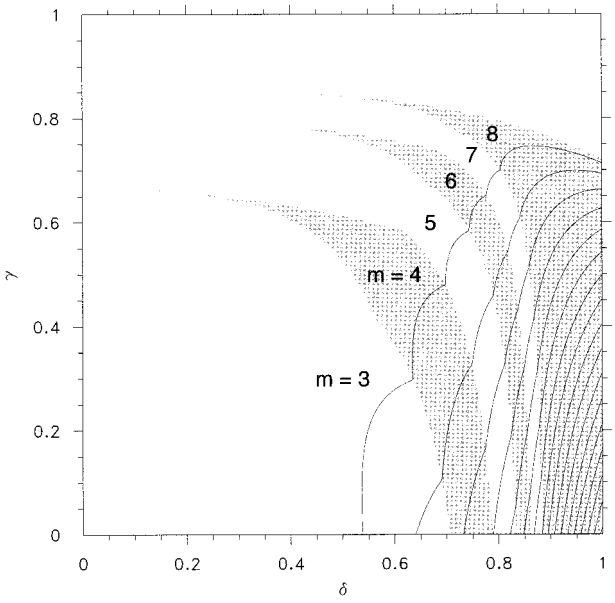

FIG. 2. Isolines of the maximum dimensionless growth rate ν_i/ζ_{av} among the tangential wavenumbers $m = 3, 4, \ldots, 8$. The displayed isolines are the same as in Fig. 1, and again the largest growth rates occur in the lower-right corner of the figure. Shading indicates the wavenumber associated with the maximum dimensionless growth rate at each point.

a vorticity mixing process generally implies nonconservation of net circulation around the mixing region. As one of our goals is to characterize the ultimate end-state of this process, we prefer a numerical method that preserves exactly the net circulation. We consequently employ a pseudospectral model with ordinary (∇^2) diffusion.

In Cartesian coordinates the equations for the f-plane barotropic nondivergent model are

$$\frac{\partial u}{\partial t} + u\frac{\partial u}{\partial x} + v\frac{\partial u}{\partial y} - fv + \frac{1}{\rho}\frac{\partial p}{\partial x} = \nu\nabla^2 u, \quad (3.1)$$

$$\frac{\partial v}{\partial t} + u\frac{\partial v}{\partial x} + v\frac{\partial v}{\partial y} + fu + \frac{1}{\rho}\frac{\partial p}{\partial y} = \nu\nabla^2 v, \quad (3.2)$$

$$\frac{\partial u}{\partial x} + \frac{\partial v}{\partial y} = 0, \quad (3.3)$$

where u and v are the eastward and northward components of velocity, p is the pressure, and ρ is the constant density. Expressing the velocity components in terms of the streamfunction by $u = -\partial\psi/\partial y$ and $v = \partial\psi/\partial x$, we can write the vorticity equation, derived from (3.1) to (3.3), as

$$\frac{\partial \zeta}{\partial t} + \frac{\partial(\psi, \zeta)}{\partial(x, y)} = \nu\nabla^2\zeta, \quad (3.4)$$

where $\zeta = \nabla^2\psi$ is the relative vorticity and $\partial(\cdot\,,\cdot\,)/\partial(x, y)$ is the Jacobian operator. Two quadratic integral properties associated with (3.4) on a closed or periodic domain are the energy and enstrophy relations

$$\frac{d\mathcal{E}}{dt} = -2\nu\mathcal{Z}, \tag{3.5}$$

$$\frac{d\mathcal{Z}}{dt} = -2\nu\mathcal{P}, \tag{3.6}$$

where $\mathcal{E} = \iint \frac{1}{2}\nabla\psi\cdot\nabla\psi\, dx\, dy$ is the energy, $\mathcal{Z} = \iint \frac{1}{2}\zeta^2\, dx\, dy$ is the enstrophy, and $\mathcal{P} = \iint \frac{1}{2}\nabla\zeta\cdot\nabla\zeta\, dx\, dy$ is the palinstrophy. The diffusion term on the right-hand side of (3.4) controls the spectral blocking associated with the enstrophy cascade to higher wavenumbers.

Although the determination of the pressure field is not required when the flow evolution is predicted by (3.4), it is nevertheless useful for physical understanding to periodically diagnose the pressure field. Forming the divergence equation from (3.1) and (3.2) one obtains

$$\frac{1}{\rho}\nabla^2 p = f\nabla^2\psi - 2\left[\left(\frac{\partial^2\psi}{\partial x\partial y}\right)^2 - \frac{\partial^2\psi}{\partial x^2}\frac{\partial^2\psi}{\partial y^2}\right]. \tag{3.7}$$

On specifying the constants f and ρ, (3.7) can then be used to determine p from ψ.

Section 4 presents a representative numerical integration of (3.4) that demonstrates the formation of polygonal eyewalls, asymmetric eye contraction, and vorticity mixing. The solutions of (3.4) to be presented were obtained with a double Fourier pseudospectral code having 512 × 512 equally spaced collocation points on a doubly periodic domain of size 600 km × 600 km. The code was run with a dealiased calculation of the quadratic advection terms in (3.4). This results in 170 × 170 Fourier modes. Although the collocation points are only 1.17 km apart, a more realistic estimate of resolution is the wavelength of the highest Fourier mode, which is 3.53 km. While the gross features of the flow evolution presented below have been confirmed using lower spatial resolution and larger computational domains, the current configuration of numerical parameters yields a good compromise between computer speed and memory limitations and the desire for an adequately resolved inertial range. Other numerical details are as follows. Time differencing was accomplished with a standard fourth-order Runge–Kutta scheme using a 7.5-s time step. The chosen value of ν was 100 $m^2\ s^{-1}$, resulting in a $1/e$ damping time of 53 min for all modes having total wavenumber 170. This damping time lengthens to 3.5 h for modes having total wavenumber 85.

4. Redistribution of PV for initially hollow PV structures

a. Initial condition

In real hurricanes we expect the instability to develop from a wide spectrum of naturally occuring background noise. Consequently, the initial condition for (3.4) consists of an azimuthally broadbanded perturbation to a circular vorticity distribution, that is,

$$\zeta(r,\phi,0) = \begin{cases} \zeta_1, & 0 \le r \le r_1 - d_1 \\ \zeta_1 S((r - r_1 + d_1)/2d_1) + \zeta_2 S((r_1 + d_1 - r)/2d_1), & r_1 - d_1 \le r \le r_1 + d_1 \\ \zeta_2, & r_1 + d_1 \le r \le r_2 - d_2 \\ \zeta_2 S((r - r_2 + d_2)/2d_2) + \zeta_3 S((r_2 + d_2 - r)/2d_2), & r_2 - d_2 \le r \le r_2 + d_2 \\ \zeta_3, & r_2 + d_2 \le r < \infty \end{cases}$$

$$+ \zeta_{\text{amp}} \sum_{m=1}^{8} \cos(m\phi) \begin{cases} 0, & 0 \le r \le r_1 - d_1 \\ S((r_1 + d_1 - r)/2d_1), & r_1 - d_1 \le r \le r_1 + d_1 \\ 1, & r_1 + d_1 \le r \le r_2 - d_2 \\ S((r - r_2 + d_2)/2d_2), & r_2 - d_2 \le r \le r_2 + d_2 \\ 0, & r_2 + d_2 \le r < \infty, \end{cases} \tag{4.1}$$

where r_1, r_2, d_1, d_2, $\zeta_1 - \zeta_3$, $\zeta_2 - \zeta_3$, and ζ_{amp} are independently specified quantities, and the constant ζ_3 is determined in order to make the domain average of $\zeta(r, \phi, 0)$ vanish. Here $S(s) = 1 - 3s^2 + 2s^3$ is the basic cubic Hermite shape function satisfying $S(0) = 1$, $S(1) = 0$, and $S'(0) = S'(1) = 0$. Sensitivity tests using other broadbanded initial asymmetries yield qualitatively similar results provided the perturbation excites a nontrivial azimuthal wavenumber one component (either initially or through wave–wave interaction).[3]

For the representative numerical experiment we set the initial condition parameters to be $r_1 = 37.5$ km, d_1

[3] For exceptional initial conditions (i.e., those that do not contain an azimuthal wavenumber 1 contribution nor excite wavenumber 1

$= 7.5$ km, $r_2 = 57.5$ km, $d_2 = 7.5$ km, $\zeta_1 - \zeta_3 = 4.1825 \times 10^{-4}$ s^{-1}, $\zeta_2 - \zeta_3 = 3.3460 \times 10^{-3}$ s^{-1}, and $\zeta_{\text{amp}} = 1.0 \times 10^{-5}$ s$^{-1} \approx 0.003\zeta_2$. To make the domain average vorticity vanish we must choose $\zeta_3 = -6.0653 \times 10^{-5}$ s^{-1}. The symmetric part of the initial vorticity, tangential wind, and angular velocity fields are shown by the solid lines in Fig. 4 (the other lines in this figure will be discussed later). The vorticity of the ring is approximately nine times the vorticity of the central region. The initial tangential wind is weak inside 35 km but increases rapidly between 40 km and 50 km, where the vorticity is large. Note that the maximum tangential wind is approximately 54 m s^{-1} and lies on the outer edge of the vorticity ring near 60-km radius. The initial angular velocity $\overline{\omega}$ is a maximum at approximately 57 km, where the vortex turnaround time, $2\pi/\overline{\omega}$, is approximately 1.9 h. The ''differential'' rotation is cyclonic inside 57 km and anticyclonic outside 57 km. A stability analysis (not shown) of this continuous vorticity distribution establishes that wavenumber 4 is the most unstable and has an *e*-folding time of 57.5 min. An approximate interpretation of this continuous vorticity distribution in terms of the three-region model yields a point in Fig. 2 near the transition between wavenumbers 4 and 3 along the line $\gamma \approx 0.20$, which also predicts en *e*-folding time just under 60 min. A detailed analysis of the direct numerical integration (Fig. 3) at early times also yields a dominant mode-4 disturbance with a consistent *e*-folding time of approximately 60 min.

b. Redistribution into a monopole

The results of the experiment are shown in the form of vorticity maps in Fig. 3 (every 2 h until $t = 24$ h and every 6 h thereafter). Near the beginning of the experiment the vorticity wave on the inner edge of the ring ($30 \leq r \leq 45$ km) is embedded in weak cyclonic flow of approximately 9 m s^{-1} ($\overline{\omega} \approx 0.25 \times 10^{-3}$ s^{-1} or 7 h circuit time) and is propagating cyclonically relative to this flow. The vorticity wave on the outer edge of the ring ($50 \leq r \leq 65$ km) is embedded in strong cyclonic flow of approximately 54 m s^{-1} ($\overline{\omega} \approx 0.92 \times 10^{-3}$ s^{-1} or 1.9 h turnaround time) and is propagating anticyclonically relative to this flow. As the two vorticity waves phase lock and help each other grow, the wave on the inner edge of the high vorticity ring is the first to reach the wave-breaking stage. During the breaking stage, interior particles with low and intermediate vorticity are drawn out into the high vorticity ring. This low and intermediate vorticity fluid spirals cyclonically into and carves up the high vorticity fluid in the original annular ring. This stretching and folding process turns the original high vorticity ring into an area of active enstrophy cascade. Two consequences of the withdrawal of intermediate and low PV fluid are a dramatic tightening of the PV gradient on the inside edge of the vorticity ring and a significant decrease in the area of the inner, low vorticity region. For example, the area of the inner, square-shaped, dark blue region at $t = 8$ h is approximately 60% of the dark blue inner area at $t = 0$ h. In other words, 40% of the low vorticity inner fluid has been mixed into the high vorticity ring. Thus, the annular ring shrinks inward and, through mixing, becomes broader and less intense. At $t = 6$ h the vorticity wave on the outer edge of the ring has increased enough in amplitude so that its four tips are in regions where the differential rotation is anticyclonic. In a period of 2 h, spiral bands form and, as vorticity is stripped off the outer edge of the high vorticity ring, the vorticity gradient is significantly tightened there also. Between 10 and 12 h the central region of low vorticity (dark blue) is knocked off-center and a long filament of it is withdrawn just to the south and east of the center of the domain. The remaining patch of low vorticity now begins to circle the vortex approximately every 2 h. For example, at 24 h it lies west-southwest of the center between $r = 35$ and 55 km. At these radii, the tangential wind is approximately 40 m s^{-1}, the orbital time is approximately 2 h, and there is weak anticyclonic differential rotation (see bottom two panels of Fig. 4).

In terms of the integral quantities enstrophy and palinstrophy, the period between 6 and 16 h is remarkable. During this period there is a large pulse of palinstrophy (5 times its initial value) and an associated [see Eq. (3.6)] rapid decay of enstrophy (as shown in Fig. 8). During these 10 h, approximately 32% of the original enstrophy is sent to small scales, where it is dissipated. In contrast, the angular momentum and kinetic energy are nearly conserved. For example, at $t = 24$ h, the angular momentum, kinetic energy, and enstropy are 99.9%, 99.2%, and 59.5% of their respective initial values.

Between 24 and 48 h the patch of low vorticity circles the vortex 10 times while the patch of high vorticity (located 30 km east-southeast of the domain center at $t = 24$ h) settles into the vortex center, accompanied by its associated trailing spiral bands of vorticity. At 48 h the nearly circular vorticity contour at the vortex center is 0.0025 s^{-1} and the central vorticity maximum is 0.0026 s^{-1}, which is 79% of the initial vorticity value in the annular ring. Thus, the fluid in the center of the vortex at 48 h should not be considered as a large patch that has been simply moved from the original vortex ring to the center under the constraint of material conservation of vorticity. Rather, the fluid in the vortex

through nonlinear interaction) the macroscopic results (not shown) are observed to be qualitatively much different. In such cases the vorticity ring never mixes completely into a monopole whose largest vorticity resides at the center. For example, if the initial perturbation is in mode 4 only, then the nonlinear interactions excite modes 8, 12, 16, ... The high vorticity in the ring thus never gets advected to the storm center due to the absence of a wavenumber 1 wind component. [The relative contribution from the mode 1 algebraic instability (see footnote 1) to the vorticity mixing process reported here for the general case of a broadbanded initial disturbance has not yet been determined.] For such exceptional initial conditions the mathematical theory developed in sections 5 and 6 is no longer applicable as it implicitly assumes no mixing barriers.

center at 48 h can be considered a mixture of some fluid which was initially in the high vorticity annular ring, some fluid which was inside this ring, and some fluid which was outside this ring. This interpretation will be further discussed in section 6, where the fractional contributions of fluid from each of the three regions will be determined via the maximum entropy hypothesis.

The symmetric (azimuthal mean) parts of the vorticity and tangential wind fields at selected times during the evolution are shown in Fig. 4. For this calculation, we take the vortex center as being the center of the domain.[4] Early on ($t = 4$ h) a slight inward flux of mean vorticity on the interior side of the vorticity ring and a slight outward flux of vorticity on the exterior side of the ring is evident. Then there is a rather sudden transition to more extensive lateral mixing. Eventually, the lateral mixing process terminates and the mean vorticity profile assumes an almost monopolar structure except for a weak sign reversal in the radial vorticity gradient near $r = 30$ km. The mean tangential winds undergo a significant structure change as well. Corresponding to the vorticity transport to the center of the vortex, the mean tangential winds in the ''eye'' region increase substantially, while the overall tangential wind maximum decreases.

As one means of assessing whether the model resolution is adequate, we show the kinetic energy and enstrophy spectra in Fig. 5 at selected times through the violent mixing phase ($0 \le t \le 16$ h). An extensive enstrophy cascade is evident around $t = 8$ h. Subsequently, the small-scale energy increases somewhat but diffusion ultimately prevents the energy from piling up near the wavenumber cutoff.

It is interesting to speculate as to the possible physical effect of such a mesoscale mixing process on the thermodynamic structure of the hurricane eye region and vortex intensity. We generally think of the hurricane eye as being so dry that mixing of air from the eye into the eyewall cloud would be detrimental to convection. However, in addition to being dry, the air in the eye is also warm, so warm in fact that the air in the eye can often have an equivalent potential temperature higher than the air in the eyewall cloud (e.g., as shown below 700 mb in Fig. 16 of Hawkins and Imbembo 1976). In such a circumstance the mixing of air from the eye into the eyewall cloud as idealized here may actually be beneficial to convection. Emanuel (1997) goes a step further by arguing that the mechanical spinup of the eye region by vorticity mixing is critical for a hurricane to achieve its maximum intensity.

c. Particle trajectories

To better understand the initial stages of the mixing process, let us now consider the stability of Lagrangian particle trajectories within the nondivergent velocity field. The trajectory $[X(t), Y(t)]$ of a single particle is calculated from $\dot{X} = -\psi_y(X, Y)$ and $\dot{Y} = \psi_x(X, Y)$. A small perturbation of the trajectory $(\delta X, \delta Y)$ evolves according to the linear system

$$\frac{d}{dt}\begin{pmatrix}\delta X\\ \delta Y\end{pmatrix} = \begin{pmatrix}-\psi_{xy} & -\psi_{yy}\\ \psi_{xx} & \psi_{xy}\end{pmatrix}\begin{pmatrix}\delta X\\ \delta Y\end{pmatrix}. \tag{4.2}$$

Searching for solutions of (4.2) of the form $e^{\lambda t}$, we find that $\lambda = \pm\sqrt{Q}$ where $Q = \psi_{xy}^2 - \psi_{xx}\psi_{yy}$. In regions where $Q < 0$, two neighboring particles do not separate exponentially in time. Defining the two components of strain by $S_1 = u_x - v_y = -2\psi_{xy}$ and $S_2 = v_x + u_y = \psi_{xx} - \psi_{yy}$, we can interpret Q as a measure of the relative magnitudes of strain and vorticity, that is, $Q = \frac{1}{4}(S_1^2 + S_2^2 - \zeta^2)$. The coherent monopolar vortices that emerge during the evolution of decaying two-dimensional turbulence (McWilliams 1984; Benzi et al. 1988) have central regions with strongly negative Q surrounded by regions of weakly positive Q.

An alternate interpretation of the Q field can be obtained by taking the x and y derivatives of (3.4). Neglecting diffusion one obtains without any approximation

$$\frac{D}{Dt}\begin{pmatrix}\zeta_x\\ \zeta_y\end{pmatrix} = \begin{pmatrix}\psi_{xy} - \psi_{xx}\\ \psi_{yy} - \psi_{xy}\end{pmatrix}\begin{pmatrix}\zeta_x\\ \zeta_y\end{pmatrix}, \tag{4.3}$$

which leads to the same eigenvalues discussed above.

The time evolution of the Q field for the numerical experiment is shown in Fig. 6. For the first 4 h the Q field remains negative everywhere within the radius of maximum wind, with a thin ring of positive values just outside the radius of maximum wind. As the wave number 4 disturbance develops, four regions of positive Q appear near $r = 40$ km, where the intermediate and low vorticity fluid is being mixed into the high vorticity ring. At $t = 8$ h, the value of Q in these four regions is approximately 1×10^{-6} s^{-2}, which corresponds to an e-folding time for particle separation, $Q^{-1/2}$, of approximately 17 min.

There is an active enstrophy cascade occurring within the ring of high vorticity. Low vorticity fluid from the interior region is drawn out into the ring in four places and subjected to continual stretching and folding. This asymmetric eye contraction mechanism is physically quite different from the symmetric eye contraction mechanism proposed by Shapiro and Willoughby (1982) and Willoughby et al. (1982). The relative importance of these symmetric and asymmetric mechanisms in actual hurricanes remains an open question.

d. A flawed heuristic argument

To emphasize the erroneous nature of simple arguments based on vorticity rearrangement without mixing, consider the situation illustrated in the upper row of Fig. 7, that is, the case of constant vorticity within the annular region $r_1 < r < r_2$. The vorticity is zero inside r_1 and outside r_2. Now imagine that all of the vorticity

[4] Since the model is on an f plane, the centroid of vorticity is invariant and always remains at the domain center.

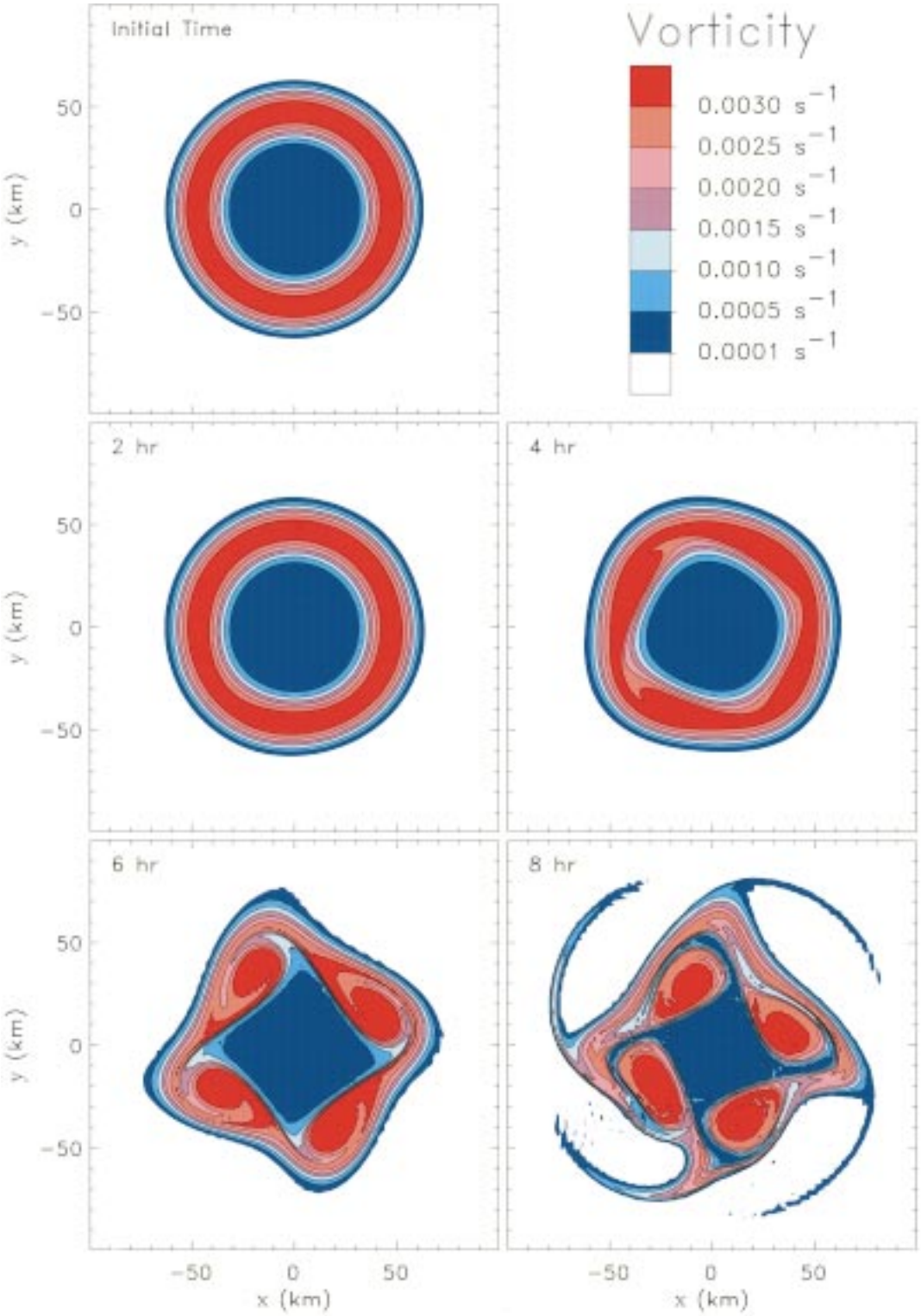

FIG. 3. Vorticity contour plots for the representative numerical experiment. The model domain is 600 km × 600 km, but only the inner 200 km × 200 km is shown. The contours begin at 0.0005 s^{-1} and are incremented by 0.0005 s^{-1}. Low vorticity values are shaded blue and high vorticity values are shaded red. (a) Vorticity from $t = 0$ h to 8 h.

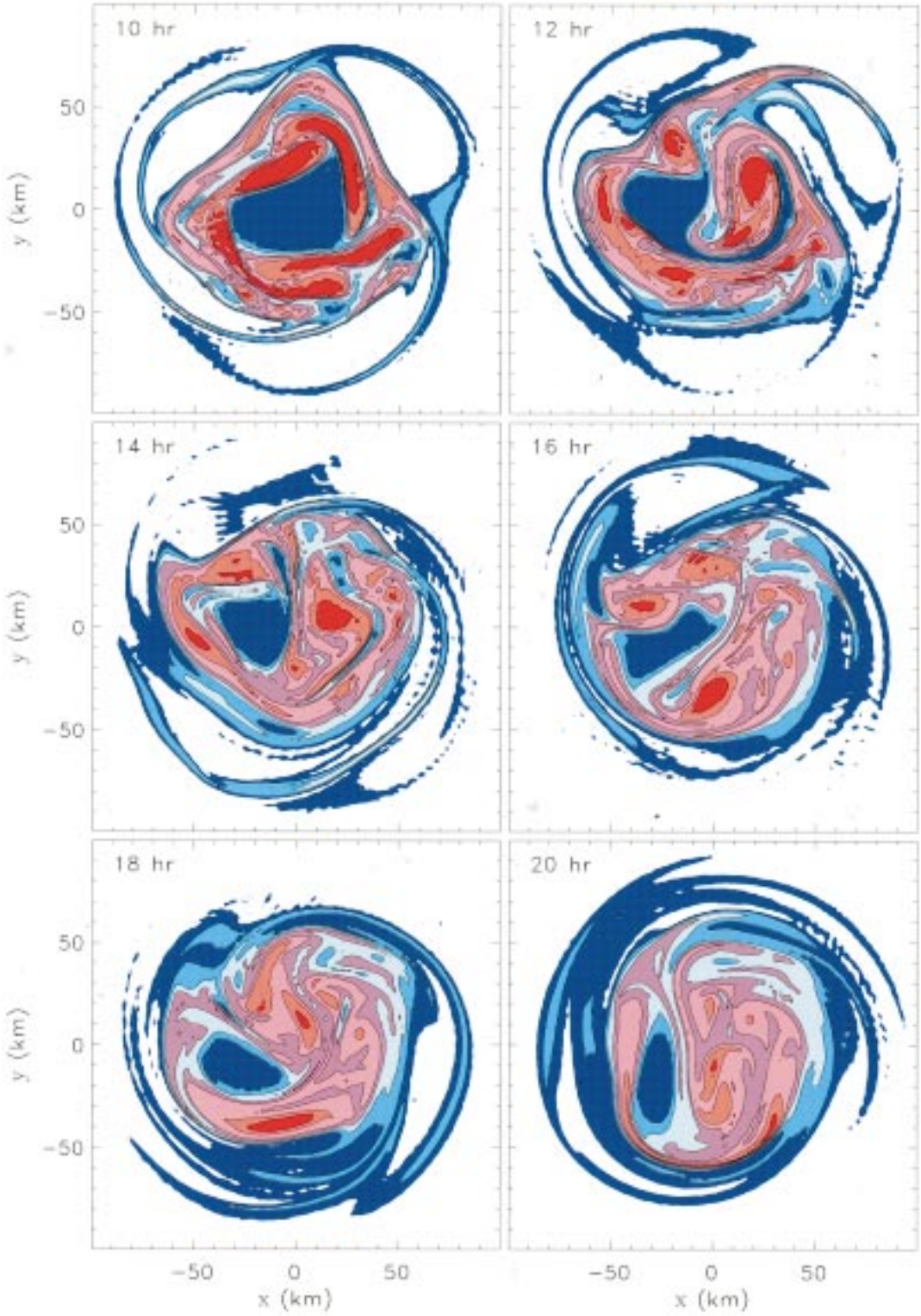

FIG. 3. (*Continued*) (b) Vorticity from t = 10 h to 20 h.

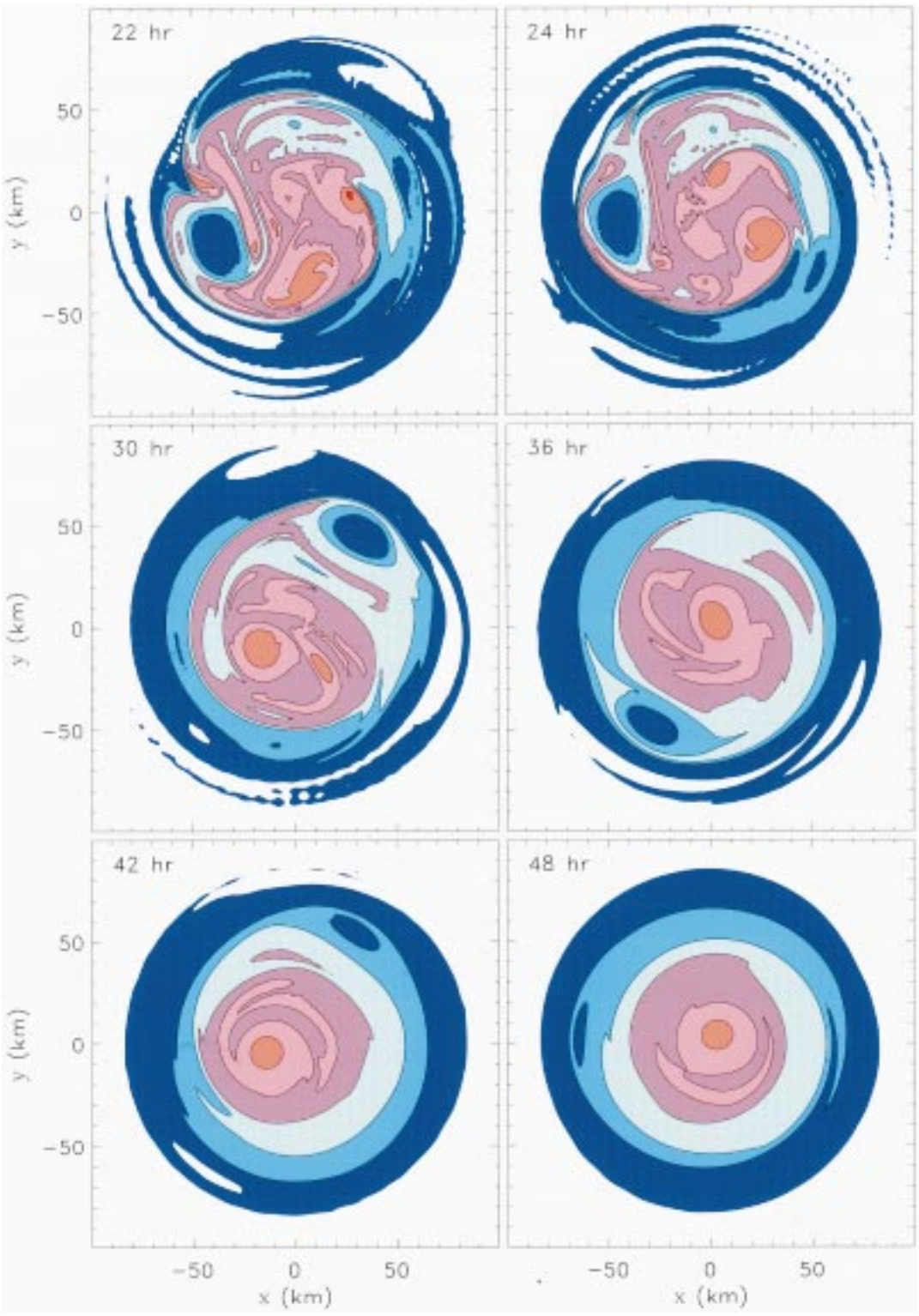

Fig. 3. (*Continued*) (c) Vorticity from $t = 22$ h to 48 h with the time interval switched to 6 h after $t = 24$ h.

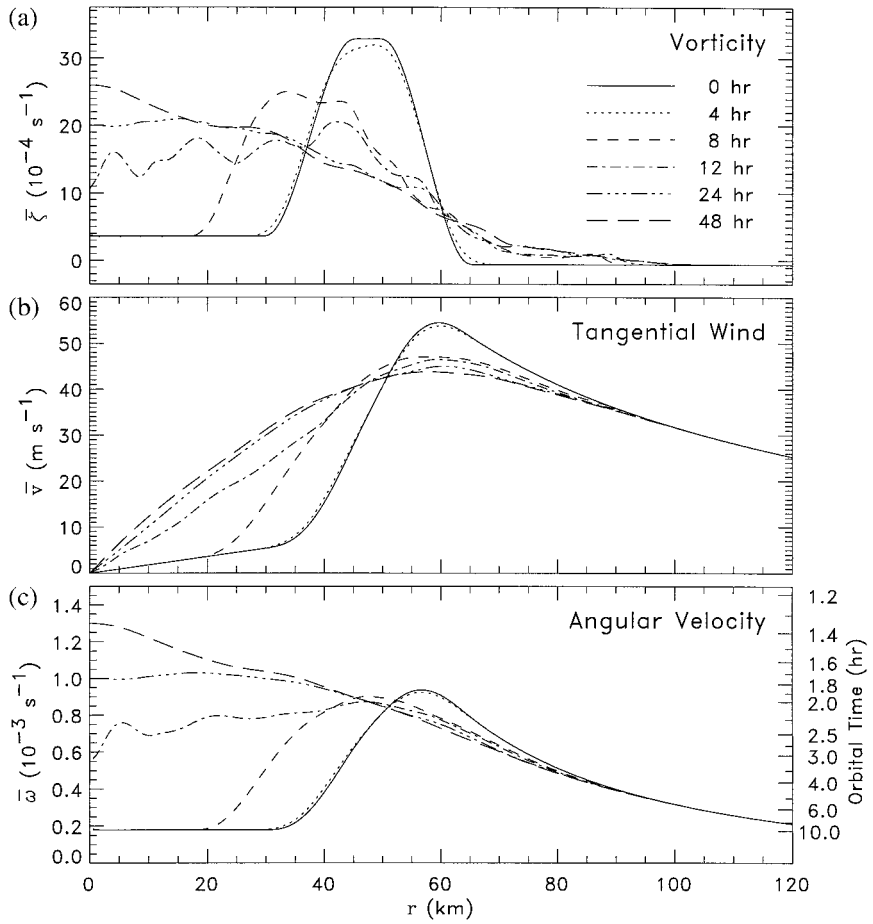

FIG. 4. Azimuthal mean vorticity ($\overline{\zeta}$), tangential velocity ($\overline{v}$), and angular velocity ($\overline{\omega}$) for the experiment shown in Fig. 3 at the selected times $t = 0$ (solid), 4 h (dotted), 8 h (dashed), 12 h (dash–dot), 24 h (dash–dot–dot–dot), 48 h (long dashes). The scale on the right of the bottom panel is for $2\pi/\overline{\omega}$, the orbital time of fluid particles (minor tick marks are for values halfway between the labeled major tick marks).

becomes redistributed, without any mixing, into a circular patch of uniform vorticity centered at $r = 0$. Let r_1, r_2, v_{max} denote the inner radius, outer radius, and maximum tangential wind at the initial time. Let R_2, V_{max} denote the corresponding values at the final time once the redistribution is complete. It is then easy to show that upon preserving the net circulation

$$V_{max} = v_{max}\frac{r_2}{(r_2^2 - r_1^2)^{1/2}} > v_{max}.$$

However, this hypothetical final flow, illustrated in the lower row of Fig. 7, has larger kinetic energy and angular momentum than the initial flow. For the redistribution process to also conserve angular momentum and/or kinetic energy, it must be accompanied by vorticity mixing and some vorticity must be thrown outward (or left behind) in filaments that orbit the vortex core. This is clearly evident in the numerical solution.

5. Analytical prediction of the equilibrated end state via the minimum enstrophy hypothesis

Two approaches have been proposed in the literature that allow one to predict the equilibrated end state without explicitly simulating the details of the time-dependent nonlinear evolution of the flow. In this section we consider the minimum enstrophy approach and in section 6 we consider the maximum entropy approach. These approaches rest on different assumptions and lead to somewhat different solutions; we discuss these differences at the end of section 6.

a. The selective decay hypothesis

An improvement to the flawed argument of section 4d that is more consistent with the nonlinear evolution shown in Fig. 3 invokes the selective decay hypothesis (e.g., Matthaeus and Montgomery 1980), which says that the barotropic instability process leads to an active

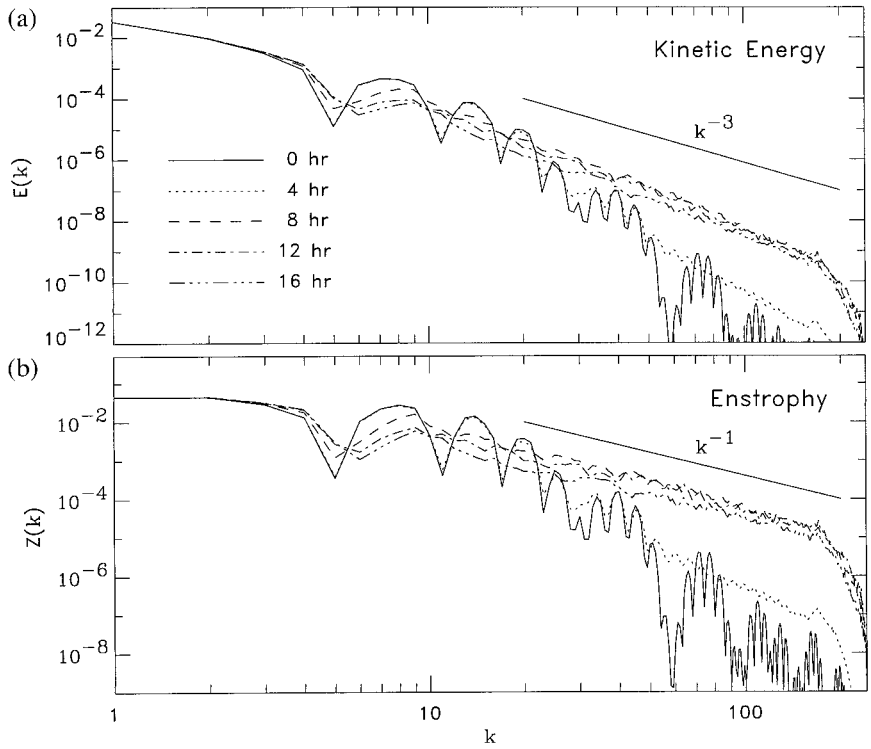

FIG. 5. Kinetic energy ($E(k)$) and enstrophy ($Z(k)$) spectra during the extensive mixing phase ($0 \leq t \leq 16$ h) for the experiment shown in Fig. 3 at the selected times $t = 0$ (solid), 4 h (dotted), 8 h (dashed), 12 h (dash–dot), and 16 h (dash–dot–dot–dot). Spectra are obtained in the usual way by binning into rings of radius k centered at the origin in Cartesian wavenumber space. The k^{-3} (energy) and k^{-1} (enstrophy) spectra, as expected for the enstrophy cascade from two-dimensional turbulence theory (neglecting logarithmic corrections), are shown for comparison.

cascade of the spectral distribution of enstrophy to high wavenumbers, where dissipation operates to decrease the enstrophy. By contrast, the area-integrated kinetic energy and angular momentum tend to be rugged integrals that are essentially unchanged.

Figure 8 shows a time series of the area-integrated kinetic energy, angular momentum, enstrophy, and palinstrophy for the numerical experiment shown in Fig. 3. Noteworthy features are the approximate invariance of the kinetic energy and angular momentum (1.4% reduction in kinetic energy and 0.1% reduction in angular momentum) over the duration of the mixing process. The enstrophy on the other hand is reduced substantially (47.4% overall), beginning near $t = 8$ h. The increase in the palinstrophy is consistent with the enstrophy decrease as must be the case from (3.6). A theory predicting the end-state of this mixing process in a dissipative (though nearly inviscid) evolution should be consistent with these properties.

Let a denote the outer edge of the vorticity mixing region. Following Leith (1984) we first hypothesize that, out of the family of vortices that have the same integrated angular momentum inside $r = a$ and the same tangential wind at each radius outside $r = a$, the vortex with minimum integrated enstrophy inside $r = a$ is the one toward which the flow actually evolves. This vortex is derived in section 5b and is called MinEV-$\mathcal{M}$, that is, the minimum enstrophy vortex with constrained circulation and angular momentum. As a second hypothesis we argue that, out of the family of vortices that have the same integrated energy inside $r = b$ and the same tangential wind at each radius outside $r = b$, the vortex with minimum integrated enstrophy inside $r = b$ is the one toward which the flow actually evolves. This vortex is called MinEV-$\mathcal{E}$, that is, the minimum enstrophy vortex with constrained circulation and energy, and is presented in section 5c.

b. Minimum enstrophy vortex with constrained circulation and angular momentum (MinEV-$\mathcal{M}$)

To begin the MinEV-$\mathcal{M}$ argument, we first note that, for the final vortex, the integrated angular momentum inside the mixing radius $r = a$ is given by $2\pi \int_0^a rvr\, dr$. Because this angular momentum integral may be unbounded as $a \to \infty$, it is convenient to work with the angular momentum deficit with respect to the initial vortex. Thus, for a vortex with initial and final tangential wind profiles $v_0(r)$ and $v(r)$, let us define the angular momentum deficit with respect to the angular momen-

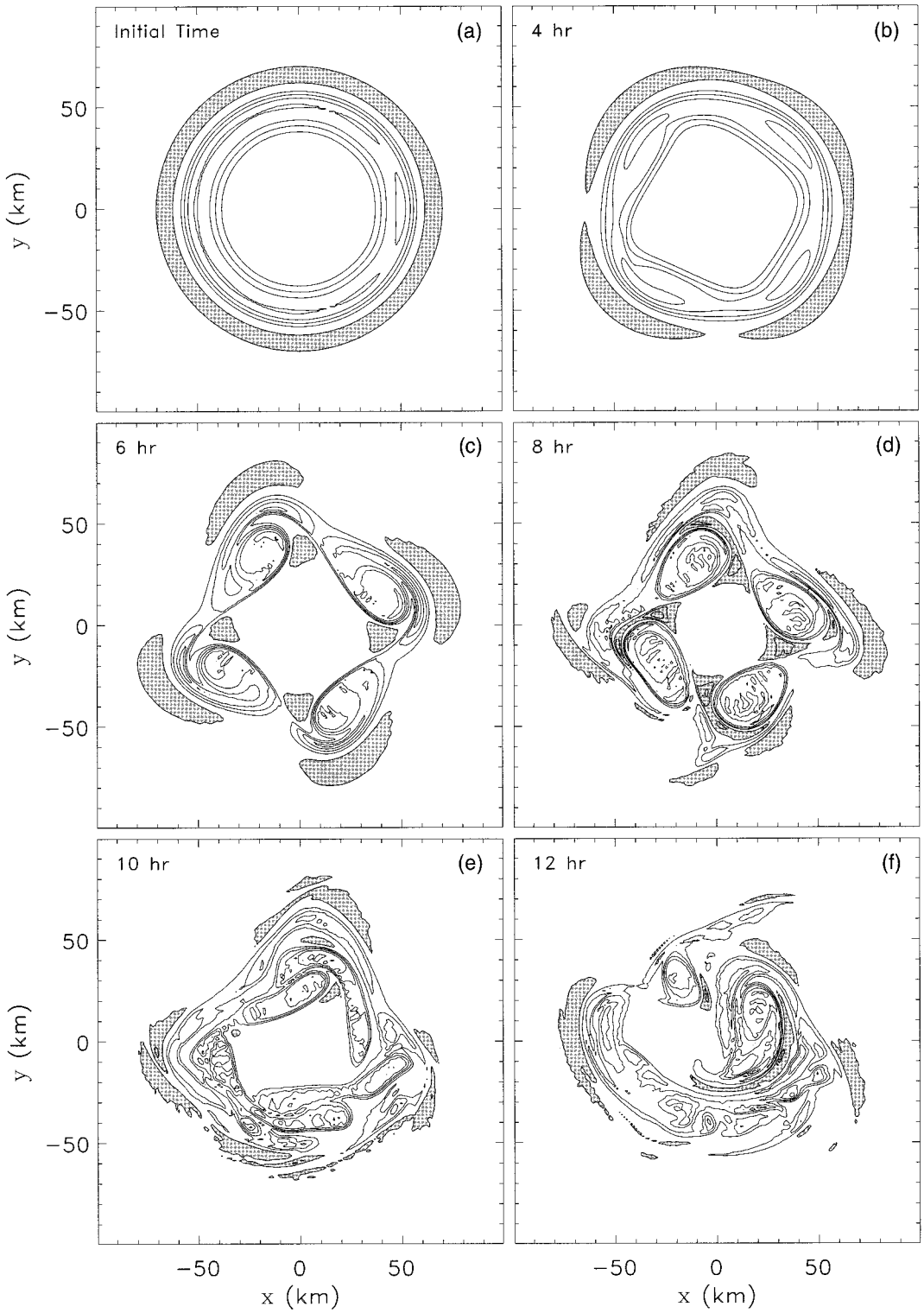

FIG. 6. Contour plots of the Q field ($Q = \psi_{xy}^2 - \psi_{xx}\psi_{yy}$) at selected times for the experiment shown in Fig. 3. The contour interval is 0.5×10^{-6} s^{-2}, with the zero isoline omitted for clarity (to suppress the effect of small oscillations about zero). The shading (where $Q \geq 0.5 \times 10^{-6}$ s^{-2}) corresponds to regions of particle separation.

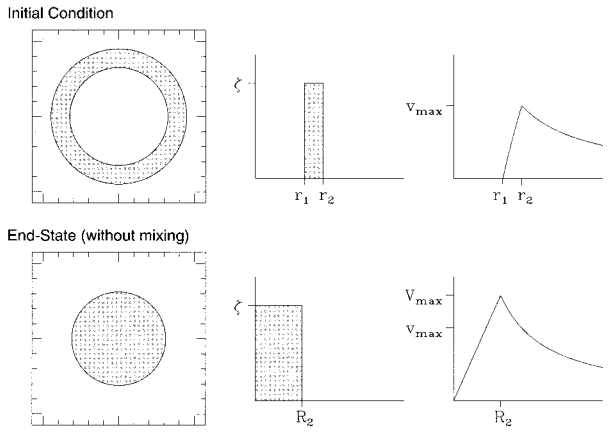

FIG. 7. Schematic of an initial vorticity distribution and the corresponding hypothesized end-state after a redistribution without mixing. The redistribution argument illustrated here is flawed because it violates kinetic energy and angular momentum invariance. This points out the necessity of vorticity mixing during the redistribution process.

tum of the initial vortex as $2\pi \int_0^a r(v_0 - v)r\,dr = \pi \int_0^a r^2(\zeta - \zeta_0)r\,dr$, where $\zeta = d(rv)/r\,dr$ and where the second form of the angular momentum deficit follows from an integration by parts. For the special case where the initial tangential wind $v_0(r)$ is the corresponding tangential flow associated with a point vortex having the same circulation as the final flow, the angular momentum deficit is proportional to the total moment, about the origin, of the force impulse required to generate the difference motion $(v - v_0)$ from rest (Batchelor 1967, section 7c). In a similar fashion, noting that all

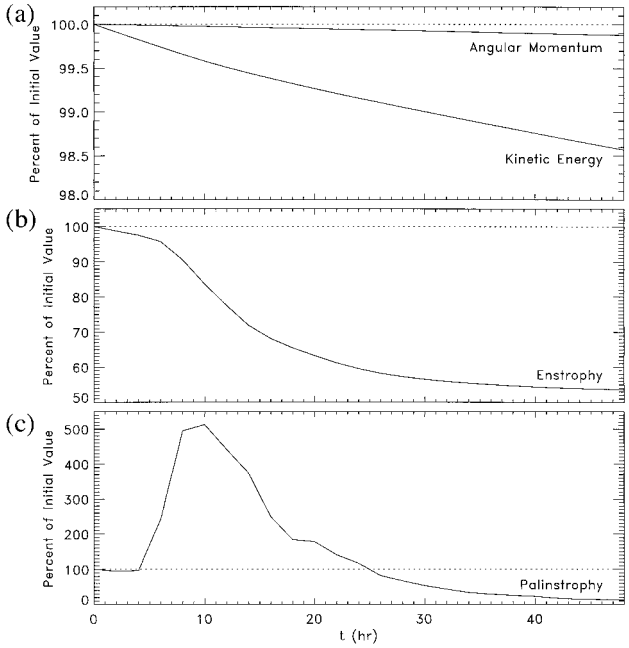

FIG. 8. Time series of kinetic energy ($\mathcal{E}$), angular momentum ($\mathcal{M}$), enstrophy ($\mathcal{Z}$), and palinstrophy ($\mathcal{P}$), all of which are integrated over the model domain for the numerical experiment shown in Fig. 3.

the enstrophy deficit is contained within $r = a$, we can write the enstrophy deficit of the hypothesized final axisymmetric flow as $\pi \int_0^a (\zeta_0^2 - \zeta^2)r\,dr$.

We now vary the radius a, the tangential wind profile $v(r)$, and the associated vorticity profile $\zeta(r)$ in search of that vortex that has maximum enstrophy deficit (i.e., minimum enstrophy) for fixed circulation and angular momentum.[5] The constancy of circulation at $r = a$ requires $v(a) = v_0(a)$. Since the mixing radius a is unknown, its first variation is related to the first variation in v at that point by $\delta v(a) = [v'_0(a) - v'(a)]\delta a = [\zeta_0(a) - \zeta(a)]\delta a$ (e.g., Fox 1987). Using these results, introducing the Lagrange multiplier γ, and recalling Leibniz's rule, the variational problem then becomes

$$
\begin{aligned}
0 &= \delta \int_0^a [\zeta_0^2 - \zeta^2 + 2\gamma r(v_0 - v)]r\,dr \\
&= 2\int_0^a (-\zeta\delta\zeta - \gamma r\delta v)r\,dr + [\zeta_0^2(a) - \zeta^2(a)]a\,\delta a \\
&= 2\int_0^a \left(\frac{d\zeta}{dr} - \gamma r\right)\delta v\, r\,dr - 2a\zeta(a)\delta v(a) \\
&\quad + [\zeta_0^2(a) - \zeta^2(a)]a\,\delta a \\
&= 2\int_0^a \left(\frac{d\zeta}{dr} - \gamma r\right)\delta v\, r\,dr + [\zeta_0(a) - \zeta(a)]^2 a\,\delta a,
\end{aligned}
\tag{5.1}
$$

where the third line follows from an integration by parts, along with the relation $\delta\zeta = d(r\delta v)/rdr$. For the independent variation δa, we obtain the transversality condition

$$\zeta(a) = \zeta_0(a). \tag{5.2}$$

For the independent variation δv, we obtain the Euler–Lagrange equation

$$\frac{d\zeta}{dr} = \gamma r \quad \text{for } 0 \le r \le a. \tag{5.3}$$

Integration of (5.3) yields $\zeta(r) = d(rv)/rdr = \zeta_0(a) - (\frac{1}{2})\gamma(a^2 - r^2)$ for $0 \le r \le a$, where the constant of integration has been chosen such that (5.2) is satisfied. One further integration of this last relation for $d(rv)/rdr$ yields $v(r) = (\frac{1}{2})r\zeta_0(a) - (\frac{1}{8})\gamma a^2 r[2 - (r/a)^2]$ for $0 \le r \le a$. The condition that the final and initial tangential winds are equal at $r = a$, that is, $v(a) = v_0(a)$, yields

$$\gamma = -\frac{4}{a^2}[\bar{\zeta}_0(a) - \zeta_0(a)], \tag{5.4}$$

[5] The variational formulation developed here and in the sequel is a slight generalization of Leith's (1984) formulation since it does not require the flow to be irrotational outside the mixing region and obtains the edge of the mixing region in terms of the initial vortex.

where $\overline{\zeta}_0(r) = 2v_0(r)/r$ is the initial average vorticity inside r. Remembering that the flow is unchanged for $r \geq a$, we can write the solution for the tangential wind as

$$v(r) = \begin{cases} v_0(a)(r/a)[2 - (r/a)^2] - \dfrac{1}{2}a\zeta_0(a)(r/a)[1 - (r/a)^2] & \text{if } 0 \leq r \leq a \\ v_0(r) & \text{if } a \leq r < \infty, \end{cases} \tag{5.5}$$

for the vorticity as

$$\zeta(r) = \begin{cases} [4v_0(a)/a][1 - (r/a)^2] + \zeta_0(a)[2(r/a)^2 - 1] & \text{if } 0 \leq r \leq a \\ \zeta_0(r) & \text{if } a \leq r < \infty, \end{cases} \tag{5.6}$$

and for the angular velocity as

$$\omega(r) = \begin{cases} \omega_0(a) + \left[\omega_0(a) - \dfrac{1}{2}\zeta_0(a)\right][1 - (r/a)^2] & \text{if } 0 \leq r \leq a \\ \omega_0(r) & \text{if } a \leq r < \infty. \end{cases} \tag{5.7}$$

It is interesting to note that the solutions (5.5)–(5.7) take a particularly simple form in the special case $\zeta_0(a) = 0$. In that case it is readily shown that the radius of maximum wind is $r = (\frac{2}{3})^{1/2}a \approx 0.8165a$, the maximum wind is $v = (4\sqrt{6}/9)v_0(a) \approx 1.089v_0(a)$, the peak vorticity is twice the average vorticity inside $r = a$ [i.e., $\zeta(0) = 4v_0(a)/a$], and the peak angular velocity is twice the angular velocity at $r = a$ [i.e., $\omega(0) = 2\omega_0(a)$].

The radius a remains to be determined. If (5.5) is substituted into the angular momentum constraint $\int_0^a rv_0 r\, dr = \int_0^a rvr\, dr$, and the integral on the right-hand side is evaluated, we obtain

$$\int_0^a rv_0 r\, dr = \frac{1}{3}a^3v_0(a) - \frac{1}{24}a^4\zeta_0(a). \tag{5.8}$$

Since the functions $v_0(r)$ and $\zeta_0(r)$ are given by the initial condition, (5.8) determines a. We can summarize the predictions of the MinEV-$\mathcal{M}$ argument as follows. Given an initial circular vortex with tangential wind $v_0(r)$ and associated vorticity $\zeta_0(r)$, first determine a from (5.8). If multiple roots exist, choose that root that maximizes the enstrophy deficit.[6] The final adjusted tangential wind profile $v(r)$, vorticity profile $\zeta(r)$, and angular velocity $\omega(r)$ are then given by (5.5), (5.6), and (5.7).[7]

Using the initial tangential wind field given by the dotted curve in the second panel of Fig. 9 (the same profile as used in the direct numerical simulation), the solution of (5.8) yields $a \approx 82.13$ km, so that the outer edge of the nonzero vorticity region shifts outward approximately 17.13 km. When this value of a is inserted into (5.5) and (5.6) we obtain the $v(r)$ and $\zeta(r)$ profiles given by the dash–dotted curves in the top two panels of Fig. 9. The associated angular velocity profile $\omega(r) = v(r)/r$ is shown in the bottom panel of Fig. 9. Note that MinEV-$\mathcal{M}$ predicts an 11 m s^{-1} decrease in tangential winds near 60-km radius and a 26 m s^{-1} increase in tangential winds near 35-km radius, all in such a way that the total angular momentum (within any disk of radius ≥ 82.13 km) is invariant.

To determine the final pressure field we integrate the gradient wind relation $\rho(f + v/r)v = dp/dr$ inward from $r = 300$ km, assuming $\rho = 1.13$ kg m^{-3}, $f = 5 \times 10^{-5}$ s^{-1}, and $p = 1000$ mb at $r = 300$ km. A plot of the resulting $p(r)$ is shown by the dash–dotted curve in the third panel of Fig. 9. The dotted curve in the third panel of Fig 9 gives the radial profile of pressure for the initial condition. Note that, even though the maximum tangential wind in MinEV-$\mathcal{M}$ is approximately 11 m s^{-1} weaker than the maximum tangential wind in the initial vortex, the central pressure in MinEV-$\mathcal{M}$ is approxi-

[6] In general, conservation of angular momentum and circulation are not sufficient to guarantee a unique solution to (5.8). For the initial vortex discussed above one finds an infinite number of roots inside the high vorticity region ($a \leq 46$ km) and a distinct root outside ($a \approx 82$ km). The root yielding the maximum enstrophy deficit (the distinct root) is deemed the solution to the MinEV-$\mathcal{M}$ problem. Although in principle it is possible that the nonlinear evolution could become frozen in one of these local enstrophy minima (see, e.g., Butler 1991), in practice we do not observe such behavior in the direct numerical simulations that relax rapidly to an equilibrium that is well described by the MinEV-$\mathcal{M}$ solution.

[7] Upon taking the second variation it can be shown that the MinEV-$\mathcal{M}$ vortex is in fact a local minimum with respect to axisymmetric variations.

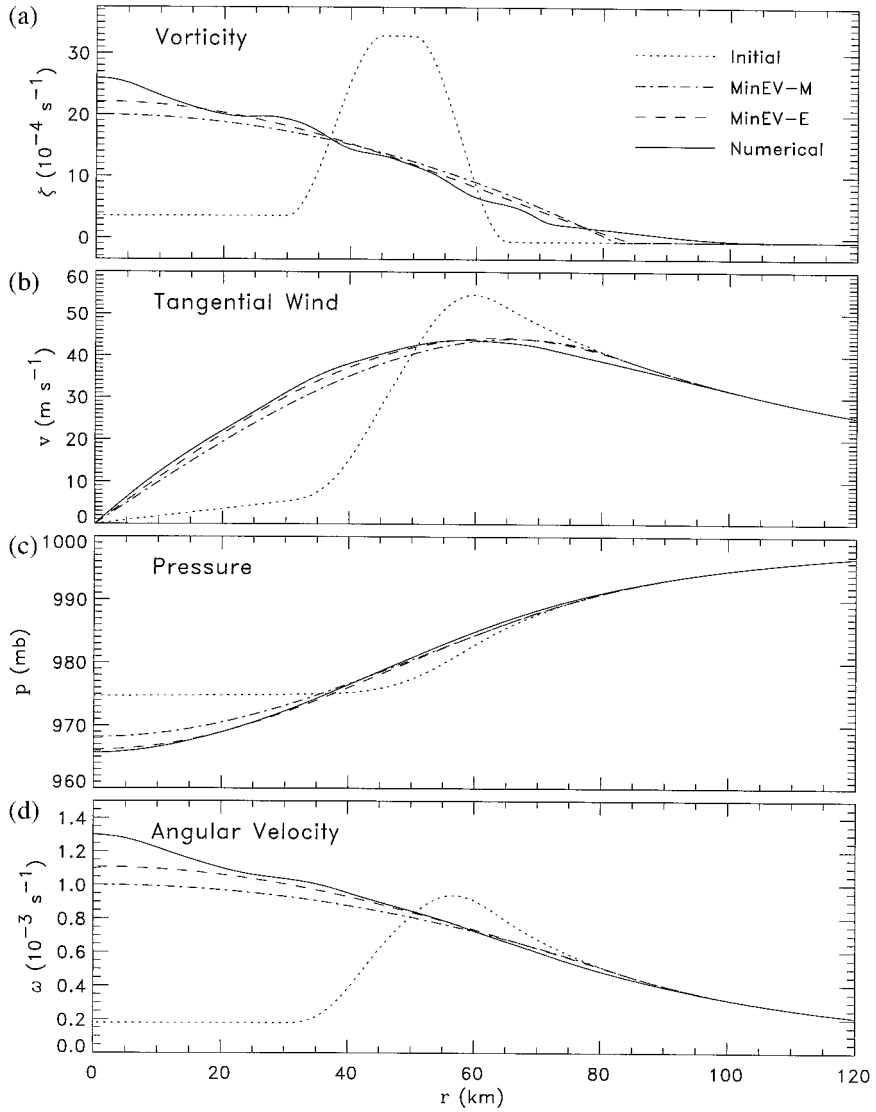

FIG. 9. Plots of the azimuthal mean vorticity $\zeta(r)$, tangential wind $v(r)$, pressure $p(r)$, as determined from gradient balance, and angular velocity $\omega(r)$ for MinEV-$\mathcal{M}$ (dash–dotted curves), MinEV-$\mathcal{E}$ (dashed curves), and the direct numerical integration at 48 h (solid curves). The initial curves are shown by the dotted lines. Note that in both cases the vortex appears to be weakening in terms of tangential wind, but strengthening in terms of central pressure.

mately 7 mb lower than the initial central pressure. In other words, MinEV-$\mathcal{M}$ looks weaker than the initial vortex when viewed in terms of maximum tangential wind, but looks stronger than the initial vortex when viewed in terms of minimum central pressure. This result cautions us about the inherent unreliability of statistical relationships between the central pressure and the maximum tangential wind in real tropical cyclones.

Since the mean vorticity inside $r = a$ is invariant, that is, $\int_0^a \zeta r\, dr = \int_0^a \zeta_0 r\, dr$, and since the angular momentum inside $r = a$ is also invariant, that is, $\int_0^a r^2\zeta r\, dr = \int_0^a r^2\zeta_0 r\, dr$, we can define an invariant mean radius $\overline{r}$ by

$$\overline{r} = \left(\frac{\int_0^a r^2\zeta r\, dr}{\int_0^a \zeta r\, dr}\right)^{1/2} = \left(\frac{\int_0^a r^2\zeta_0 r\, dr}{\int_0^a \zeta_0 r\, dr}\right)^{1/2}. \quad (5.9)$$

The mean radius $\overline{r}$ is a measure of the dispersion of the vorticity about $r = 0$. For MinEV-$\mathcal{M}$, $\overline{r}$ is strictly conserved from the initial to the final vortex. Using (5.6) in (5.9) we obtain $\overline{r} = a\{(\frac{1}{3})[1 + a\zeta_0(a)/(4v_0(a))]\}^{1/2} \approx 46.7$ km. Thus, in the top panel of Fig. 9, $\overline{r} \approx 46.7$ km is the mean radius of the vorticity dispersion for both the initial ζ profile and the final ζ profile predicted

by the MinEV-$\mathcal{M}$ argument. Since $\bar{r}$ is so constrained, it is easy to see how a small outward mixing of vorticity by spiral bands and filaments must be accompanied by a much larger inward mixing of vorticity by asymmetric eye contraction. In this sense the outward mixing of vorticity by spiral bands in real hurricanes (which we often can observe with radar) may be indicative of inner-core vorticity mixing which is difficult to observe because of the absence of strong radar scattering there.

c. Minimum enstrophy vortex with constrained circulation and energy (MinEV-$\mathcal{E}$)

To begin the MinEV-$\mathcal{E}$ argument, we first note the energy deficit inside $r = b$ is given by $\pi \int_0^b (v_0^2 - v^2) r\, dr$. We assume that, in the region $r \geq b$, the final axisymmetric flow $v(r)$ is equal to the initial axisymmetric flow $v_0(r)$. In a similar fashion, noting that all the enstrophy deficit is contained within $r = b$, we can write the enstrophy deficit of the hypothesized final axisymmetric flow as $\pi \int_0^b (\zeta_0^2 - \zeta^2) r\, dr$.

We now vary the radius b, the tangential wind profile $v(r)$, and the associated vorticity profile $\zeta(r)$ in search of that vortex that has maximum enstrophy deficit for fixed energy. Because the derivation parallels the derivation of the MinEV-$\mathcal{M}$ vortex, the details are provided in the appendix. The resulting tangential wind is given by

$$v(r) = \begin{cases} v_0(b) J_1(\mu r)/J_1(\mu b) & \text{if } 0 \leq r \leq b \\ v_0(r) & \text{if } b \leq r < \infty, \end{cases} \tag{5.10}$$

and the relative vorticity is given by

$$\zeta(r) = \begin{cases} v_0(b) \mu J_0(\mu r)/J_1(\mu b) & \text{if } 0 \leq r \leq b \\ \zeta_0(r) & \text{if } b \leq r < \infty, \end{cases} \tag{5.11}$$

where J_0 and J_1 denote Bessel functions of the first kind of order zero and one, respectively. The unknowns μ and b are determined from the requirements that ζ be continuous at $r = b$, that is, $\zeta(b) = \zeta_0(b)$, and that energy be conserved, that is, $\int_0^b v_0^2(r) r\, dr = \int_0^b v^2(r) r\, dr$. For the initial tangential wind profile given by the dotted curve in Fig. 9, we find that $\mu \approx 0.02912$ km^{-1} and $b \approx 84.42$ km, so that the outer edge of the nonzero vorticity region shifts outward approximately 19.42 km. The final $v(r)$ and $\zeta(r)$ profiles are given by the dashed curves in the top two panels of Fig. 9. The associated angular velocity profile $\omega(r) = v(r)/r$ is shown in the bottom panel of Fig. 9. Note that the tangential winds predicted by MinEV-$\mathcal{E}$ are generally within 1 or 2 m s^{-1} of the tangential winds predicted by MinEV-$\mathcal{M}$.

To determine the final pressure field we again integrate the gradient wind relation inward from $r = 300$ km, assuming $\rho = 1.13$ kg m^{-3}, $f = 5 \times 10^{-5}$ s^{-1}, and $p = 1000$ mb at $r = 300$ km. The resulting pressure $p(r)$ is plotted as the dashed line in the third panel of Fig. 9. Note that the central pressure in MinEV-$\mathcal{E}$ is approximately 9 mb lower than the initial central pressure.

Also shown in Fig. 9 are the tangential mean $\zeta(r)$, $v(r)$, $p(r)$, $\omega(r)$ for the direct numerical integration at 48 h (solid curves). A comparison of the MinEV-$\mathcal{M}$ and MinEV-$\mathcal{E}$ curves with the solid curves shows that the predictions of the two MinEV theories agree well with the direct numerical integration for this example. Unfortunately, the predictions of the two MinEV theories are not always so reliable. The next section develops an alternative theory, based on maximizing a mixing entropy; the strengths and weaknesses of the two approaches are contrasted in subsection 6c.

6. Analytical prediction of the equilibrated end-state via the maximum entropy principle

The direct numerical simulation shown in Fig. 3 illustrates how the mixing process can produce vorticity patterns of increasing intricacy. An adaptive numerical method, such as contour dynamics, requires an increasing amount of computer time to advance one time step as the vorticity field becomes more complex. On the other hand, the pseudospectral method used to produce Fig. 3 is not adaptive and requires a fixed amount of computer time to advance one time step, no matter how complex the vorticity field. In spectral methods the production of finer and finer scales in vorticity is arrested by the model resolution and by the diffusion (or hyperdiffusion) processes operating near the resolution limit. While it is tempting to run spectral models at higher and higher resolution in order to follow vorticity structures to finer and finer scales, such costly pursuits do not necessarily yield fundamental advances in our understanding of the dynamics. A statistical mechanics approach may be more useful. Using the standard point-vortex model, Persing and Montgomery (1995) simulated the evolution of perturbed vortex rings as a way of determining the final radial vorticity profile in statistical equilibrium. A theoretical approach applicable to continuous vorticity distributions and based on the maximum entropy principle has recently been developed by Miller (1990), Robert (1991), Robert and Sommeria (1991, 1992), Sommeria et al. (1991), Miller et al. (1992), Whitaker and Turkington (1994), Chavanis and Sommeria (1996), and Turkington and Whitaker (1996). Although the maximum entropy theory suffers from the weakness of predicting vortex merger when the 2D Euler equations predict corotation without merger (Whitaker and Turkington 1994), one nevertheless hopes that the theory makes reliable predictions when mixing processes are dominant. As a test of the theory and as a foundation for future work we present here a simple version of this maximum entropy argument for the unforced vortex mixing problem.

a. Tertiary mixing case

The maximum entropy argument rests on two views of the vorticity field after mixing: a macroscopic view,

which sees a smooth distribution of vorticity, and a microscopic view, which reveals the intricate details produced by stretching and folding of vorticity in nonlinear flow. Rather than attempting to describe the finescale distribution (''microstate'') directly, we represent the macroscopic vorticity at a point statistically by averaging over all possible microstates in a small neighborhood of the point.

To keep the mathematics tractable, we assume that the end-state is axisymmetric and that the initial state is given by

$$\zeta_0(r) = \begin{cases} \zeta_1 & \text{if } 0 \le r < r_1 \\ \zeta_2 & \text{if } r_1 \le r < r_2 \\ \zeta_3 & \text{if } r_2 \le r < \infty, \end{cases}$$

where r_1, r_2, ζ_1, ζ_2, and ζ_3 are specified constants. With this initial condition the problem reduces to one of tertiary mixing. Suppose we sample the vorticity at N points within a small neighborhood of r. Let n_1 denote the number of points at which the vorticity value ζ_1 is found, n_2 the number of points at which the vorticity value ζ_2 is found, and $N - n_1 - n_2$ the number of points at which the vorticity value ζ_3 is found. Then $\rho_1(r) = n_1/N$ denotes the probability, at point r, of finding the vorticity ζ_1, $\rho_2(r) = n_2/N$ the probability of finding the vorticity ζ_2, and $\rho_3(r) = 1 - \rho_1(r) - \rho_2(r)$ the probability of finding vorticity ζ_3. The number of possible arrangements having n_1 points with vorticity ζ_1, n_2 points with vorticity ζ_2, and $N - n_1 - n_2$ points with vorticity ζ_3 is the multiplicity function W, which is given by

$$W = \frac{N!}{n_1!n_2!(N - n_1 - n_2)!}.$$

The logarithm of the multiplicity function is $\ln W = \ln N! - \ln n_1! - \ln n_2! - \ln(N - n_1 - n_2)!$. Using the Stirling approximation (e.g., $\ln N! \approx N \ln N - N$ for large N), we obtain

$$\begin{aligned} \ln W &\approx N \ln N - n_1 \ln n_1 - n_2 \ln n_2 \\ &\quad - (N - n_1 - n_2) \ln(N - n_1 - n_2) \\ &= -n_1 \ln(n_1/N) - n_2 \ln(n_2/N) \\ &\quad - (N - n_1 - n_2) \ln(1 - n_1/N - n_2/N), \end{aligned}$$

and we conclude that the entropy density is given by

$$\lim_{N\to\infty} \left(\frac{1}{N} \ln W\right) = -\rho_1 \ln\rho_1 - \rho_2 \ln\rho_2 - (1 - \rho_1 - \rho_2) \ln(1 - \rho_1 - \rho_2).$$

Isolines of the entropy density in the (ρ_1, ρ_2) plane for $\rho_1 \ge 0$ and $\rho_2 \ge 0$ with $\rho_1 + \rho_2 \le 1$ are shown in Fig. 10. Note that the entropy density $-\rho_1 \ln\rho_1 - \rho_2 \ln\rho_2 - (1 - \rho_1 - \rho_2) \ln(1 - \rho_1 - \rho_2)$ approaches zero as $(\rho_1, \rho_2) \to (0, 0)$, (0, 1), (1, 0), and that its maximum value of ln3 occurs at $\rho_1 = \rho_2 = \frac{1}{3}$. In other words the multiplicity of microstates is a maximum when a third of the sampled points in the neighborhood of r have vorticity ζ_1, a third have vorticity ζ_2, and a third have vorticity ζ_3.

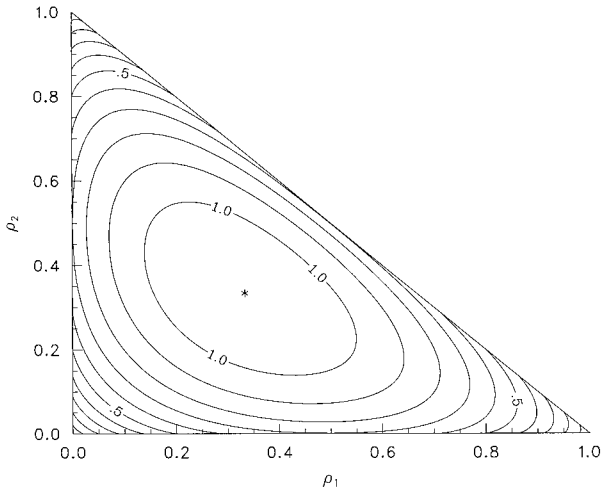

FIG. 10. Isolines of the entropy density $-\rho_1 \ln\rho_1 - \rho_2 \ln\rho_2 - (1 - \rho_1 - \rho_2) \ln(1 - \rho_1 - \rho_2)$ in the (ρ_1, ρ_2)-plane for $\rho_1 \ge 0$ and $\rho_2 \ge 0$ with $\rho_1 + \rho_2 \le 1$. The isolines are 0.1, 0.2, . . . , 1.0 and the asterisk indicates the maximum value of entropy density (ln 3), which occurs at $\rho_1 = \rho_2 = \frac{1}{3}$.

We now define the Boltzmann mixing entropy $S[\rho_1(r), \rho_2(r)]$ as

$$\begin{aligned} &S[\rho_1(r), \rho_2(r)] \\ &= \int_0^\infty [-\rho_1 \ln\rho_1 - \rho_2 \ln\rho_2 - (1 - \rho_1 - \rho_2) \\ &\qquad \times \ln(1 - \rho_1 - \rho_2)] r\, dr. \end{aligned} \tag{6.1a}$$

The functional $S[\rho_1(r), \rho_2(r)]$ measures the loss of information in going from the fine grain (microscopic) view to the coarse grain (macroscopic) view. The macroscopic vorticity is given in terms of $\rho_1(r)$ and $\rho_2(r)$ by $\zeta(r) = \zeta_1\rho_1(r) + \zeta_2\rho_2(r) + \zeta_3[1 - \rho_1(r) - \rho_2(r)]$. To find the most probable macroscopic state, we must find the particular $\rho_1(r)$ and $\rho_2(r)$, which maximize $S[\rho_1(r), \rho_2(r)]$ subject to all the integral constraints associated with the inviscid vorticity dynamics. In other words, the variational problem is to find the expectation functions $\rho_1(r)$ and $\rho_2(r)$ by maximizing (6.1a) subject to the circulation constraints

$$\int_0^\infty \zeta_1\rho_1(r) r\, dr = \int_0^{r_1} \zeta_0(r) r\, dr, \tag{6.1b}$$

$$\int_0^\infty \zeta_2\rho_2(r) r\, dr = \int_{r_1}^{r_2} \zeta_0(r) r\, dr, \tag{6.1c}$$

the energy constraint

$$\int_0^\infty \frac{1}{2}(v^2 - v_0^2)r\,dr = 0, \tag{6.1d}$$

and the angular momentum constraint

$$\int_0^\infty (rv - rv_0)r\,dr = 0. \tag{6.1e}$$

Defining $\tilde{\zeta}_1 = \zeta_1 - \zeta_3$ and $\tilde{\zeta}_2 = \zeta_2 - \zeta_3$, and introducing the Lagrange multipliers α_1, α_2, β, γ, the variational problem is

$$\begin{aligned} 0 = \delta \int_0^\infty \Big[& -\rho_1 \ln\rho_1 - \rho_2 \ln\rho_2 \\ & - (1 - \rho_1 - \rho_2)\ln(1 - \rho_1 - \rho_2) + \alpha_1\rho_1 \\ & + \alpha_2\rho_2 + \frac{1}{2}\beta(v^2 - v_0^2) + \gamma(rv - rv_0)\Big] r\,dr \\ = \int_0^\infty \Big[& -\ln\left(\frac{\rho_1}{1 - \rho_1 - \rho_2}\right)\delta\rho_1 - \ln\left(\frac{\rho_2}{1 - \rho_1 - \rho_2}\right)\delta\rho_2 \\ & + \alpha_1\delta\rho_1 + \alpha_2\delta\rho_2 + \beta v\delta v + \gamma r\delta v\Big] r\,dr \\ = \int_0^\infty & \left[-\ln\left(\frac{\rho_1}{1 - \rho_1 - \rho_2}\right) + \alpha_1 - \tilde{\zeta}_1\left(\beta\psi + \frac{1}{2}\gamma r^2\right)\right]\delta\rho_1 r\,dr \\ = \int_0^\infty & \left[-\ln\left(\frac{\rho_2}{1 - \rho_1 - \rho_2}\right) + \alpha_2 - \tilde{\zeta}_2\left(\beta\psi + \frac{1}{2}\gamma r^2\right)\right]\delta\rho_2 r\,dr, \end{aligned} \tag{6.2}$$

where the last equality in (6.2) results from an integration by parts, along with the relations $v = d\psi/dr$ and $\delta\zeta = d(r\delta v)/r dr = \tilde{\zeta}_1\delta\rho_1 + \tilde{\zeta}_2\delta\rho_2$. For arbitrary variations $\delta\rho_1$ and $\delta\rho_2$, we obtain

$$\ln\left(\frac{\rho_1}{1 - \rho_1 - \rho_2}\right) = \alpha_1 - \tilde{\zeta}_1\left(\beta\psi + \frac{1}{2}\gamma r^2\right) \tag{6.3a}$$

and

$$\ln\left(\frac{\rho_2}{1 - \rho_1 - \rho_2}\right) = \alpha_2 - \tilde{\zeta}_2\left(\beta\psi + \frac{1}{2}\gamma r^2\right). \tag{6.3b}$$

Solving (6.3) for $\rho_1(r)$ and $\rho_2(r)$, we obtain

$$\rho_1(r) = \frac{\exp\left[\alpha_1 - \tilde{\zeta}_1\left(\beta\psi + \frac{1}{2}\gamma r^2\right)\right]}{1 + \exp\left[\alpha_1 - \tilde{\zeta}_1\left(\beta\psi + \frac{1}{2}\gamma r^2\right)\right] + \exp\left[\alpha_2 - \tilde{\zeta}_2\left(\beta\psi + \frac{1}{2}\gamma r^2\right)\right]}, \tag{6.4a}$$

$$\rho_2(r) = \frac{\exp\left[\alpha_2 - \tilde{\zeta}_2\left(\beta\psi + \frac{1}{2}\gamma r^2\right)\right]}{1 + \exp\left[\alpha_1 - \tilde{\zeta}_1\left(\beta\psi + \frac{1}{2}\gamma r^2\right)\right] + \exp\left[\alpha_2 - \tilde{\zeta}_2\left(\beta\psi + \frac{1}{2}\gamma r^2\right)\right]}. \tag{6.4b}$$

Using $\zeta(r) = \zeta_1\rho_1(r) + \zeta_2\rho_2(r) + \zeta_3[1 - \rho_1(r) - \rho_2(r)]$, we obtain

$$\frac{d}{rdr}\left(r\frac{d\psi}{dr}\right) = \tilde{\zeta}_1\rho_1(r) + \tilde{\zeta}_2\rho_2(r) + \zeta_3. \tag{6.4c}$$

Since the expectation functions $\rho_1(r)$ and $\rho_2(r)$ are given by (6.4a,b), Eq. (6.4c) is a nonlinear ordinary differential equation for $\psi(r)$ with yet to be determined Lagrange multipliers α_1, α_2, β, γ. The equations for α_2, α_2, β, γ are obtained by enforcing the constraints (6.1b)–(6.1e). Thus, evaluating the integrals on the right-hand sides of (6.1b) and (6.1c), we obtain

$$\int_0^\infty \rho_1(r)r\,dr = \frac{1}{2}r_1^2, \tag{6.4d}$$

$$\int_0^\infty \rho_2(r)r\,dr = \frac{1}{2}(r_2^2 - r_1^2). \tag{6.4e}$$

The energy constraint (6.1d) can also be written as $\int_0^\infty \psi(\zeta - \zeta_3)r\,dr = \int_0^{r_2} \psi_0(\zeta_0 - \zeta_3)r\,dr$. When the integral on the right-hand side of this form of the energy constraint is evaluated, we obtain

$$\begin{aligned} \int_0^\infty & \psi[\tilde{\zeta}_1\rho_1(r) + \tilde{\zeta}_2\rho_2(r)]r\,dr \\ & = \frac{1}{16}\{\tilde{\zeta}_1\zeta_1 r_1^4 + \tilde{\zeta}_2 \\ & \quad \times [\zeta_2(r_2^4 - r_1^4) - 4(\zeta_2 - \zeta_1)r_1^2 r_2^2 \ln(r_2/r_1)]\}. \end{aligned} \tag{6.4f}$$

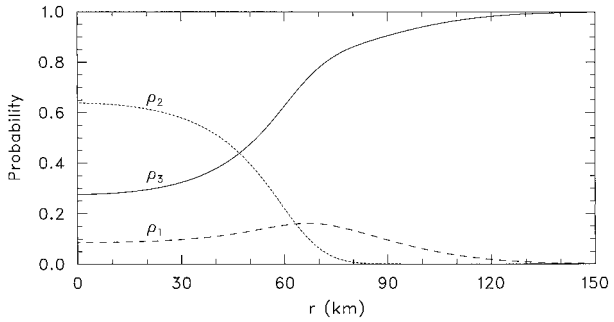

FIG. 11. The MaxSV expectation functions $\rho_1(r)$ (dashed), $\rho_2(r)$ (dotted), and $\rho_3(r) = 1 - \rho_1(r) - \rho_2(r)$ (solid), as computed from (6.4a)–(6.4g) for the initial condition displayed by the thick solid curves in Fig. 12.

Similarly, the angular momentum constraint (6.1e) can be written as $\int_0^\infty r^2(\zeta - \zeta_3)r\,dr = \int_0^{r_2} r^2\,(\zeta_0 - \zeta_3)r\,dr$. When the integral on the right-hand side of this form of the angular momentum constraint is evaluated, we obtain

$$\int_0^\infty r^2[\tilde{\zeta}_1\rho_1(r) + \tilde{\zeta}_2\rho_2(r)]r\,dr = \frac{1}{4}r_1^4\tilde{\zeta}_1 + \frac{1}{4}(r_2^4 - r_1^4)\tilde{\zeta}_2. \quad (6.4g)$$

In summary, the solution of the maximum entropy vortex problem involves solving the seven equations comprising the nonlinear system (6.4) for $\rho_1(r)$, $\rho_2(r)$, $\psi(r)$, α_1, α_2, β, γ, given the constants r_1, r_2, ζ_1, ζ_2, ζ_3.

Analytical solutions of the system (6.4) are not easily obtained, and numerical methods are generally required. To solve (6.4) we have used the iterative algorithm developed by Turkington and Whitaker (1996). For the constants defining the initial condition, we choose $r_1 = 37.5$ km, $r_2 = 57.5$ km, $\tilde{\zeta}_1 = 4.1825 \times 10^{-4}$ s^{-1}, $\tilde{\zeta}_2 = 3.3460 \times 10^{-3}$ s^{-1}, $\zeta_3 = -6.0653 \times 10^{-5}$ s^{-1}. This is the three region approximation to the initial condition used in the direct numerical simulation described in section 4. When these constants are used, the numerical solution of (6.4) yields the radial profiles of $\rho_1(r)$, $\rho_2(r)$, and $\rho_3(r) = 1 - \rho_1(r) - \rho_2(r)$ shown in Fig. 11. These profiles can be interpreted as follows. In the MaxSV end-state, fluid particles from the initial annular ring have the highest probability (~64%) of ending up in the central core, while fluid particles from the initial core have the highest probability (~16%) of ending up just outside the initial annular ring near $r = 67$ km. In the central core of the MaxSV end-state there is a higher probability of finding air that was originally outside the annular ring (~28%) than finding air that was originally inside the annular ring (~9%). In this sense, the vortex has been ''turned inside-out.'' Such intense inside-out turning is the typical fate of highly unstable initial vortices with very low central vorticity. In contrast, for weakly unstable initial vortices whose central vorticity

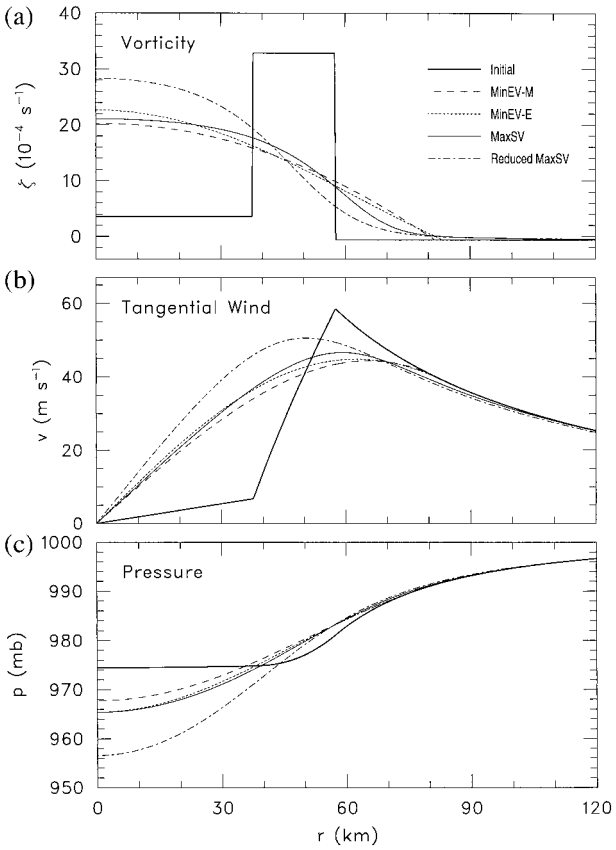

FIG. 12. A comparison of the predictions of MinEV-$\mathcal{M}$ (dashed) and MinEV-$\mathcal{E}$ (dotted) with the predictions of complete MaxSV (thin solid) and reduced MaxSV (dash–dotted). The initial curves are shown by the thick solid lines.

is only slightly lower than the vorticity of the annular ring, the amount of mixing is predicted to be much less, and typically $\rho_1 > \rho_3$ at $r = 0$.

The resulting vorticity profile, computed from $\zeta(r) = \zeta_1\rho_1(r) + \zeta_2\rho_2(r) + \zeta_3[1 - \rho_1(r) - \rho_2(r)]$, is shown by the thin solid line in the top panel of Fig. 12. The MaxSV-predicted reduction (~37%) in the maximum vorticity value from the initial condition to the final state is a consequence of the fundamental mixing processes occurring during the flow evolution. This emphasizes the fact that material conservation of vorticity on the macroscale is not a useful description of the flow evolution, even though material conservation of vorticity on the microscale is a useful description.

The integration of this vorticity profile yields the tangential wind profile shown by the thin solid line in the middle panel of Fig. 12. The corresponding pressure field, computed from the gradient balance relation as in sections 5b and 5c, is shown by the thin solid line in the bottom panel. For comparison, the MinEV-$\mathcal{M}$ and MinEV-$\mathcal{E}$ solutions for this same initial condition are also shown in the three panels of Fig. 12. For this particular initial condition the predictions of MaxSV, MinEV-$\mathcal{M}$, and MinEV-$\mathcal{E}$ are all very similar, and, as

implied by Fig. 9, all agree quite well with the direct numerical simulation. However, as is discussed below in section 6c, the MaxSV theory gives more reliable predictions over a wide range of initial conditions.

b. Maximum entropy vortex with constrained circulation and angular momentum only

The maximum entropy theory for tertiary mixing has four Lagrange multipliers (α_1, α_2, β, γ) and four constraints [the circulation constraints (6.4d), (6.4e), the energy constraint (6.4f), and the angular momentum constraint (6.4g)]. Can we obtain essentially equivalent solutions if we drop one of the constraints and, hence, one of the Lagrange multipliers? We have found that the answer to this question is, in many cases, no. To illustrate, consider the solution obtained when the energy constraint (6.4f) and the Lagrange multiplier β are dropped from the problem. Note that this significantly simplifies the problem (6.4) since the $\beta\psi$ terms disappear from (6.4a), (6.4b) and the determination of α_1, α_2, γ via (6.4d), (6.4e), (6.4g) decouples from the determination of ψ via (6.4c). Using the same values of r_1, r_2, $\tilde{\zeta}_1$, $\tilde{\zeta}_2$, ζ_3 given in section 6a, we now obtain from this reduced MaxSV theory the radial profiles of $\zeta(r)$, $v(r)$, and $p(r)$ shown by the dash–dotted curves in Fig. 12. As is evident from Fig. 12, this reduced version of MaxSV theory produces less mixing, and hence higher central vorticity, than the complete MaxSV theory. The differences are large enough to conclude that this particular reduced form of MaxSV theory is not a useful approximation to the complete MaxSV theory.

c. Comparison of the MinEV and MaxSV theories

The MinEV and MaxSV approaches for predicting the final end-state of the barotropically unstable vorticity ring rest on different assumptions. For the initial basic state of Fig. 4, both produce solutions that agree well with the direct numerical solutions. However, for the tertiary mixing case, as the radial width of the initial annular vorticity patch gets larger, the MinEV-$\mathcal{M}$ and MinEV-$\mathcal{E}$ theories begin to produce unreasonably large final vorticity (i.e., larger than the initial maximum vorticity in the annular ring) near the center of the vortex. This occurs even in the case of an initially stable Rankine vortex ($r_1 = 0$) where little or no adjustment is expected.[8] The final vorticity profiles suggest that the MinEV-$\mathcal{M}$ and MinEV-$\mathcal{E}$ adjustment processes remove too much enstrophy at the outer edge of the initial vortex patch and must then produce the spuriously high vorticity near the center in order to conserve circulation.

In contrast, the maximum entropy adjustment process does not produce spuriously large vorticity, as can be seen as follows. Since $\zeta(r) = \zeta_1\rho_1(r) + \zeta_2\rho_2(r) + \zeta_3[1 - \rho_1(r) - \rho_2(r)]$ with $0 \le \rho_1(r) \le 1$, $0 \le \rho_2(r) \le 1$, $\rho_1(r) + \rho_2(r) \le 1$, the final vorticity $\zeta(r)$ is a mixture of ζ_1, ζ_2, ζ_3. In such a mixture it is impossible for the final vorticity to lie outside the range set by the maximum and minimum values of ζ_1, ζ_2, ζ_3. In this sense the predictions of the maximum entropy theory are more reliable than those of the minimum enstrophy theory.

While the MaxSV approach does not suffer from the same weaknesses of the MinEV approach for describing the redistribution of an initial vorticity ring, the MaxSV approach, when applied to atmospheric vortex merger problems, does not appear to be entirely defect-free either, since it predicts vortex merger when the 2D Euler equations predict corotation without merger (Whitaker and Turkington 1994).[9]

7. Concluding remarks

Although considerable insight into the physics of tropical cyclones has been acquired using axisymmetric theory and models (e.g., Ooyama 1969), fundamental questions remain concerning the role of asymmetric processes in the cyclone life cycle. Questions associated with asymmetric potential vorticity redistribution in tropical cyclones can be studied with a hierarchy of dynamical models. These include the barotropic nondivergent model, the barotropic divergent model (shallow water equations), the quasigeostrophic model, the asymmetric balance model, the quasi-static primitive equation model, and the full nonhydrostatic primitive equation model. The latter two models may include parameterized or explicit moist physical processes. The present study complements recent work examining tropical cyclogenesis as a PV redistribution problem governed by vortex Rossby waves on PV monopoles (Montgomery and Enagonio 1998) and has focused on PV redistribution in or near the eyewall region of mature hurricanes possessing an elevated ring of PV near the eyewall. For simplicity, the study has been limited to the barotropic nondivergent model. We thus have bypassed all questions associated with vertical structure and moist physical processes. Despite these limitations, the results seem sufficiently interesting to warrant further study with more complete physical models.

In the numerical simulations presented here, a ring of elevated vorticity was perturbed with azimuthally

[8] This fact is readily demonstrated for both the MinEV-$\mathcal{M}$ and MinEV-$\mathcal{E}$ formulations developed in sections 5b and 5c. In the former case one obtains a 33% increase in vorticity at the center while in the latter case one obtains a 40% increase.

[9] Note added in proof: A recent paper by Chavanis and Sommeria (1998) has generalized Leith's MinEV theory to simultaneously enforce the circulation, angular momentum, and energy constraints. They have shown that the resulting relation between vorticity and streamfunction is the same as the linearized version of the corresponding MaxSV relation (e.g., the linearized version of (6.4a)–(6.4c) for the three region case), thus establishing a connection between MinEV and MaxSV theories in the limit of strong mixing.

broadbanded initial conditions as a means of demonstrating a simple dynamical mechanism for the formation of polygonal eyewalls, asymmetric eye contraction, and vorticity redistribution. The intent was not to replicate the evolution of a hurricane eyewall, but rather to isolate the fundamental dynamics believed responsible for the formation of polygonal eyewalls and mesovortices. The simulations indicate that the barotropic instability associated with annular regions of relatively high vorticity results in polygonal shapes before the ultimate rearrangement into a nearly monopolar circular vortex. Although the minimum enstrophy description tends to overestimate the degradation of the maximum vorticity, the numerically simulated end-state nevertheless suggests a significant reduction of the initial vorticity maximum. These results suggest a limitation of the idea that the vorticity within the ''core'' of vortices is a rugged invariant (Carnevale et al. 1992). Analytical predictions based on maximum entropy arguments support this view.

In the eyewall of a real hurricane, frictional convergence, and moist convection continually act to concentrate high vorticity there, thus satisfying the necessary condition for barotropic exponential instability and the sufficient condition for a mode-1 algebraic instablitiy (see footnote 2). Natural convective asymmetries near the eyewall provide the perturbations that allow these instabilities to grow. As the instabilities grow the vorticity pools into a small number of ''pockets,'' creating the appearance of a polygon on the inner edge of the original annular region. These pools or pockets of PV are also likely to be responsible for mesovortices. At later times in the numerical simulations most of the vorticity in these pockets gets strained by the mean shear and is ultimately diffused by viscosity at small scales. The remaining high vorticity gets advected into the central region, thereby spinning up the center or ''eye.'' Our numerical and analytical results therefore suggest an explicit quasi-two-dimensional mechanism for the spinup and maintenance of the hurricane's eye circulation and thermal structure (via thermal wind balance), which is thought to be a crucial process for the attainment of maximum intensity (Emanuel 1997, and references).

There are a variety of ways the present work could be extended. Within the context of the barotropic nondivergent model, the theoretical predictions of sections 5 and 6 could be extended from the symmetric to the asymmetric case. Of particular interest would be the determination of the bifurcations between the symmetric and asymmetric structures predicted by the maximum entropy vortex arguments. Outside the context of the nondivergent model, both the direct numerical integrations and the theoretical predictions could be generalized to the shallow water equations. This generalization would allow a distinction between vorticity and potential vorticity and a distinction between enstrophy and potential enstrophy, and would allow the energy constraint to include both kinetic and potential energy. The generalization to the quasi-static primitive equations in isentropic coordinates would not be significantly more difficult than the shallow water case. Finally, there remains the question of the relevance of the concepts presented here to the moist convective environment in real hurricanes (e.g., Schade 1994; Guinn and Schubert 1994). This difficult question might partially be answered through the use of PV diagnostics on the output of ''full-physics models.''

In closing we would like to point out that, in addition to the connections with tornado suction vortices and with the dynamic instability of the stratospheric polar vortex (e.g., Ishioka and Yoden 1994, 1995; Bowman and Chen 1994), there is a remarkable connection between the PV redistribution problem in hurricanes and the electron density redistribution problem recently studied in experimental plasma physics. The plasma experiment involves the creation of a confined pure electron plasma in a cylindrical trap, with a uniform axial magnetic field providing radial confinement, and bias voltages applied to the cylinder ends providing axial confinement. Once produced, the confined plasma evolves due to the drift flow, which is determined by the cross product of the electric and magnetic fields (i.e., $\mathbf{E} \times \mathbf{B}$ drift). The drift flow is two-dimensional in a plane perpendicular to the axis of the cylinder. Since the drift velocity changes the electron density according to an equation identical to the inviscid form of the vorticity equation (3.4), and since electron density is related to the Laplacian of the electrostatic potential, the two-dimensional equations for the evolution of the electron plasma are isomorphic with the two-dimensional Euler equations for inviscid incompressible flow (electron density $\leftrightarrow$ vorticity and electrostatic potential $\leftrightarrow$ streamfunction). Compared to laboratory experiments with ordinary fluids (e.g., Chomaz et al. 1988), the electron plasma experiments have the advantage of being able to simulate very high Reynolds number flow; this strengthens the analogy with geophysical fluid dynamics. For further details on these extraordinary experiments readers are referred to the recent papers by Peurrung and Fajans (1993), Huang and Driscoll (1994), and Fine et al. (1995).

Acknowledgments. This work was supported in part by the National Science Foundation, under Grants ATM-9422525 and ATM-9529295, and by the Office of Naval Research under Grant ONR-N00014-93-1-0456. We also acknowledge the hospitality and support provided by the Isaac Newton Institute for Mathematical Sciences during the 1996 Program in The Mathematics of Atmosphere and Ocean Dynamics, where we benefited greatly from discussions with Chuck Leith, Rick Salmon, and Phil Morrison. We would also like to express our thanks to Paul Reasor and Mark Hidalgo for their assistance with the stability analysis of continuous profiles, and to Lloyd Shapiro and to an anonymous reviewer for their helpful comments.

APPENDIX

Derivation of the MinEV-$\mathcal{E}$ Vortex

This appendix presents the derivation of the MinEV-$\mathcal{E}$ vortex discussed in section 5c. Introducing the Lagrange multiplier λ, the variational problem is

$$\begin{aligned} 0 &= \delta \int_0^b [\zeta_0^2 - \zeta^2 + \lambda(v_0^2 - v^2)]r\, dr \\ &= 2\int_0^b (-\zeta\delta\zeta - \lambda v\delta v)r\, dr + [\zeta_0^2(b) - \zeta^2(b)]b\delta b \\ &= 2\int_0^b \left(\frac{d\zeta}{dr} - \lambda v\right)\delta v r\, dr - 2b\zeta(b)\delta v(b) \\ &\quad + [\zeta_0^2(b) - \zeta^2(b)]b\delta b \\ &= 2\int_0^b \left(\frac{d\zeta}{dr} - \lambda v\right)\delta v r\, dr + [\zeta_0(b) - \zeta(b)]^2 b\delta b, \end{aligned} \tag{A.1}$$

where (as in the MinEV-$\mathcal{M}$ case) the last term in the second line of (A.1) has been simplified by the use of $v(b) = v_0(b)$, the third line of (A.1) results from an integration by parts, along with the relation $\delta\zeta = d(r\delta v)/rdr$, and the last line makes use of $\delta v(b) = [\zeta_0(b) - \zeta(b)]\delta b$. For the independent variation δb, we obtain the transversality condition

$$\zeta(b) = \zeta_0(b). \tag{A.2}$$

For the independent variation δv, we obtain $d\zeta/dr = \lambda v$ for $0 \le r \le b$, or

$$r^2\frac{d^2v}{dr^2} + r\frac{dv}{dr} + (\mu^2 r^2 - 1)v = 0 \quad \text{for } 0 \le r \le b, \tag{A.3}$$

where $\mu^2 = -\lambda$. The solution of (A.3) is a constant times $J_1(\mu r)$, where J_1 is the first-order Bessel function. The constant is determined by requiring that $v(b) = v_0(b)$. Remembering that the flow is unchanged for $r \ge b$, we can write the solution for the tangential wind as

$$v(r) = \begin{cases} v_0(b)J_1(\mu r)/J_1(\mu b) & \text{if } 0 \le r \le b \\ v_0(r) & \text{if } b \le r < \infty. \end{cases} \tag{A.4}$$

Since $\zeta(r) = d(rv)/rdr$ and $d[rJ_1(\mu r)]/rdr = \mu J_0(\mu r)$, we obtain from (A.4)

$$\zeta(r) = \begin{cases} v_0(b)\mu J_0(\mu r)/J_1(\mu b) & \text{if } 0 \le r \le b \\ \zeta_0(r) & \text{if } b \le r < \infty. \end{cases} \tag{A.5}$$

Requiring $\zeta(b) = \zeta_0(b)$ for the expression in the upper half of (A.5) yields

$$J_0(\mu b) = \frac{\zeta_0(b)}{\mu v_0(b)}J_1(\mu b), \tag{A.6}$$

which provides one of the two necessary relations between μ and b. Another relation between μ and b is obtained as follows. Substituting (A.4) into the energy constraint $\int_0^b v_0^2(r)r\, dr = \int_0^b v^2(r)r\, dr$ yields

$$\int_0^b v_0^2(r)r\, dr = \frac{v_0^2(b)}{J_1^2(\mu b)}\int_0^b J_1^2(\mu r)r\, dr. \tag{A.7}$$

Using $xJ_1^2(x) = d\{\frac{1}{2}x^2[J_0^2(x) + J_1^2(x)] - xJ_0(x)J_1(x)\}/dx$ and (A.6), we can perform the integration in (A.7) to obtain

$$\frac{2}{b^2}\int_0^b v_0^2(r)r\, dr = v_0^2(b)\left\{1 + \frac{\zeta_0(b)}{\mu v_0(b)}\left[\frac{\zeta_0(b)}{\mu v_0(b)} - \frac{2}{\mu b}\right]\right\}. \tag{A.8}$$

Given the initial tangential wind $v_0(r)$ and the associated initial vorticity $\zeta_0(r)$, (A.6) and (A.8) determine μ and b.

An important special case of (A.6) and (A.8) occurs when the initial vorticity vanishes at those radii to which mixing extends. In that case the term in braces in (A.8) becomes unity, and b is entirely determined by (A.8). In addition, (A.6) simplifies to $J_0(\mu b) = 0$, so that μb must be one of the zeroes of the J_0 Bessel function. The minimum enstrophy will occur for the smallest possible value of μ. Thus, to minimize the enstrophy, we must choose μb to be the first zero of J_0, so that $\mu b \approx 2.4048$. From (A.4) it can then be shown that the radius of maximum wind is $r \approx 0.7656b$ and that the maximum wind is $v \approx 1.121v_0(b)$. Evaluating (A.5) at $r = 0$, we also obtain $\zeta(0) = [\mu b/2J_1(\mu b)](2v_0(b)/b) \approx 2.3161(2v_0(b)/b)$, so that the peak vorticity is approximately 2.3161 times the average vorticity inside $r = b$.

We can summarize the MinEV-$\mathcal{E}$ argument as follows. Given an initial unstable symmetric vortex with tangential wind $v_0(r)$, first determine μ and b from (A.6) and (A.8). The final adjusted tangential wind profile $v(r)$ and vorticity profile $\zeta(r)$ are then given by (A.4) and (A.5).

REFERENCES

Batchelor, G. K., 1967: *An Introduction to Fluid Dynamics*. Cambridge University Press, 615 pp.

Benzi, R., S. Patarnello, and P. Santangelo, 1988: Self-similar coherent structures in two-dimensional decaying turbulence. *J. Phys. A: Math. Gen.*, **21,** 1221–1237.

Black, P. G., and F. D. Marks, 1991: The structure of an eyewall meso-vortex in Hurricane Hugo (1989). Preprints, *19th Conf. on Hurricanes and Tropical Meteorology,* Miami, FL, Amer. Meteor. Soc., 579–582.

Bowman, K. P., and P. Chen, 1994: Mixing by barotropic instability in a nonlinear model. *J. Atmos. Sci.*, **51,** 3692–3705.

Butler, K. M., 1991: Equilibration and optimal excitation in viscous shear flow. Ph.D. dissertation, Harvard University, 133 pp. [Available from Dept. of Earth and Planetary Sciences, Harvard University, Cambridge, MA 02138.]

Carnevale, G. F., J. C. McWilliams, Y. Pomeau, J. B. Weiss, and W. R. Young, 1992: Rates, pathways and end states of nonlinear evolution in decaying two-dimensional turbulence: Scaling theory versus selective decay. *Phys. Fluids A,* **4,** 1314–1316.

Chavanis, P. H., and J. Sommeria, 1996: Classification of self-organized vortices in two-dimensional turbulence: The case of a bounded domain. *J. Fluid Mech.,* **314,** 267–297.

——, and ——, 1988: Classification of robust isolated vortices in two-dimensional hydrodynamics. *J. Fluid Mech.,* **356,** 259–296.
Chomaz, J. M., M. Rabaud, C. Basdevant, and Y. Couder, 1988: Experimental and numerical investigation of a forced circular shear layer. *J. Fluid Mech.,* **187,** 115–140.
Dritschel, D. G., 1986: The nonlinear evolution of rotating configurations of uniform vorticity. *J. Fluid Mech.,* **172,** 157–182.
——, 1988: Contour surgery: A topological reconnection scheme for extended integrations using contour dynamics. *J. Comput. Phys.,* **77,** 240–266.
——, 1989: On the stabilization of a two-dimensional vortex strip by adverse shear. *J. Fluid Mech.,* **206,** 193–221.
Eliassen, A., and M. Lystad, 1977: The Ekman layer of a circular vortex. A numerical and theoretical study. *Geophys. Norv.,* **31,** 1–16.
Emanuel, K. A., 1997: Some aspects of hurricane inner-core dynamics and energetics. *J. Atmos. Sci.,* **54,** 1014–1026.
Fine, K. S., A. C. Cass, W. G. Flynn, and C. F. Driscoll, 1995: Relaxation of 2D turbulence to vortex crystals. *Phys. Rev. Lett.,* **75,** 3277–3280.
Finley, C., 1997: Numerical simulation of intense multi-scale vortices generated by supercell thunderstorms. Ph.D. dissertation, Dept. of Atmospheric Science, Colorado State University, 297 pp. [Available from Dept. of Atmospheric Science, Colorado State University, Fort Collins, CO 80523.]
Fox, C., 1987: *An Introduction to the Calculus of Variations.* Dover, 271 pp.
Fujita, T. T., K. Watanabe, K. Tsuchiya, and M. Shimada, 1972: Typhoon-associated tornadoes in Japan and new evidence of suction vortices in a tornado near Tokyo. *J. Meteor. Soc. Japan,* **50,** 431–453.
Gall, R. L., 1982: Internal dynamics of tornado-like vortices. *J. Atmos. Sci.,* **39,** 2721–2736.
——, 1983: A linear analysis of the multiple vortex phenomenon in simulated tornadoes. *J. Atmos. Sci.,* **40,** 2010–2024.
Guinn, T. A., 1992: A dynamical theory for hurricane spiral bands. Ph.D. dissertation, Dept. of Atmospheric Science, Colorado State University, 178 pp. [Available from Dept. of Atmospheric Science, Colorado State University, Fort Collins, CO 80523.]
——, and W. H. Schubert, 1993: Hurricane spiral bands. *J. Atmos. Sci.,* **50,** 3380–3403.
——, and W. H. Schubert, 1994: Reply. *J. Atmos. Sci.,* **51,** 3545–3546.
Hasler, A. F., P. G. Black, V. M. Karyampudi, M. Jentoft-Nilsen, K. Palaniappan, and D. Chesters, 1997: Synthesis of eyewall mesovortex and supercell convective structures in Hurricane Luis with *GOES-8/9* stereo, concurrent 1-min *GOES-9* and NOAA airborne radar observations. Preprints, *22d Conf. on Hurricanes and Tropical Meteorology,* Ft. Collins, CO, Amer. Meteor. Soc., 201–202.
Hawkins, H. F., and S. M. Imbembo, 1976: The structure of a small, intense hurricane—Inez 1966. *Mon. Wea. Rev.,* **104,** 418–442.
Huang, X.-P., and C. F. Driscoll, 1994: Relaxation of 2D turbulence to a metaequilibrium near the minimum enstrophy state. *Phys. Rev. Lett.,* **72,** 2187–2190.
Ishioka, K., and S. Yoden, 1994: Nonlinear evolution of a barotropically unstable circumpolar vortex. *J. Meteor. Soc. Japan,* **72,** 63–80.
——, and ——, 1995: Nonlinear aspects of a barotropically unstable polar vortex in a forced-dissipative system: Flow regimes and tracer transport. *J. Meteor. Soc. Japan,* **73,** 201–212.
Kurihara, Y., 1976: On the development of spiral bands in a tropical cyclone. *J. Atmos. Sci.,* **33,** 940–958.
Leith, C. E., 1984: Minimum enstrophy vortices. *Phys. Fluids,* **27,** 1388–1395.
Lewis, B. M., and H. F. Hawkins, 1982: Polygonal eye walls and rainbands in hurricanes. *Bull. Amer. Meteor. Soc.,* **63,** 1294–1300.
Lin, S.-J., 1992: Contour dynamics of tornado-like vortices. *J. Atmos. Sci.,* **49,** 1745–1756.
Matthaeus, W. H., and D. Montgomery, 1980: Selective decay hypothesis at high mechanical and magnetic Reynolds numbers. *Ann. N. Y. Acad. Sci.,* **357,** 203–222.
McInytre, M. E., 1993: Isentropic distributions of potential vorticity and their relevance to tropical cyclone dynamics. *ICSU/WMO International Symposium on Tropical Cyclone Disasters,* Z. Zheng, G. Holland, and K. Emanuel, Eds., Peking University Press, 143–156.
McWilliams, J. C., 1984: The emergence of isolated coherent vortices in turbulent flow. *J. Fluid Mech.,* **146,** 21–43.
Michalke, A., and A. Timme, 1967: On the inviscid instability of certain two-dimensional vortex-type flows. *J. Fluid Mech.,* **29,** 647–666.
Miller, J., 1990: Statistical mechanics of Euler equations in two dimensions. *Phys. Rev. Lett.,* **65,** 2137–2140.
——, P. B. Weichman, and M. C. Cross, 1992: Statistical mechanics, Euler's equations, and Jupiter's red spot. *Phys. Rev. A,* **45,** 2328–2359.
Möller, J. D., and R. K. Smith, 1994: The development of potential vorticity in a hurricane-like vortex. *Quart. J. Roy. Meteor. Soc.,* **120,** 1255–1265.
Montgomery, M. T., and L. J. Shapiro, 1995: Generalized Charney-Stern and Fjørtoft theorems for rapidly rotating vortices. *J. Atmos. Sci.,* **52,** 1829–1833.
——, and R. J. Kallenbach, 1997: A theory for vortex Rossby waves and its application to spiral bands and intensity changes in hurricanes. *Quart. J. Roy. Meteor. Soc.,* **123,** 435–465.
——, and J. Enagonio, 1998: Tropical cyclogenesis via convectively forced vortex Rossby waves in a three-dimensional quasigeostrophic model. *J. Atmos. Sci.,* **55,** 3176–3207.
Muramatsu, T., 1986: The structure of polygonal eye of a typhoon. *J. Meteor. Soc. Japan,* **64,** 913–921.
Ooyama, K., 1969: Numerical simulation of the life cycle of tropical cyclones. *J. Atmos. Sci.,* **26,** 3–40.
Persing, J., and M. T. Montgomery, 1995: A point-vortex application to vortex stability, evolution and statistical equilibrium. Atmospheric Science Paper 587, Dept. of Atmospheric Science, Colorado State University, 86 pp. [Available from Dept. of Atmospheric Science, Colorado State University, Fort Collins, CO 80523.]
Peurrung, A. J., and J. Fajans, 1993: Experimental dynamics of an annulus of vorticity in a pure electron plasma. *Phys. Fluids A,* **5,** 493–499.
Ritchie, E., and G. J. Holland, 1993: On the interaction of tropical cyclone scale vortices. Part II: Discrete vortex patches. *Quart. J. Roy. Meteor. Soc.,* **119,** 1363–1379.
Robert, R., 1991: A maximum-entropy principle for two-dimensional perfect fluid dynamics. *J. Stat. Phys.,* **65,** 531–551.
——, and J. Sommeria, 1991: Statistical equilibrium states for two-dimensional flows. *J. Fluid Mech.,* **229,** 291–310.
——, and ——, 1992: Relaxation towards a statistical equilibrium state in two-dimensional perfect fluid dynamics. *Phys. Rev. Lett.,* **69,** 2776–2779.
Rotunno, R., 1982: A numerical simulation of multiple vortices. *Intense Atmospheric Vortices,* L. Bengtsson and M. J. Lighthill, Eds., Springer-Verlag, 215–228.
——, 1984: An investigation of a three-dimensional asymmetric vortex. *J. Atmos. Sci.,* **41,** 283–298.
Schade, L. R., 1994: Comments on ''Hurricane spiral bands.'' *J. Atmos. Sci.,* **51,** 3543–3544.
Shapiro, L. J., 1996: The motion of Hurricane Gloria: A potential vorticity diagnosis. *Mon. Wea. Rev.,* **124,** 2497–2508.
——, and H. E. Willoughby, 1982: The response of balanced hurricanes to local sources of heat and momentum. *J. Atmos. Sci.,* **39,** 378–394.
——, and J. L. Franklin, 1995: Potential vorticity in Hurricane Gloria. *Mon. Wea. Rev.,* **123,** 1465–1475.
Smith, R. A., and M. N. Rosenbluth, 1990: Algebraic instability of hollow electron columns and cylindrical vortices. *Phys. Rev. Lett.,* **64,** 649–652.

Snow, J. T., 1978: On inertial instability as related to the multiple-vortex phenomenon. *J. Atmos. Sci.,* **35,** 1660–1677.

Sommeria, J., C. Staquet, and R. Robert, 1991: Final equilibrium state of a two-dimensional shear layer. *J. Fluid Mech.,* **233,** 661–689.

Staley, D. O., and R. L. Gall, 1979: Barotropic instability in a tornado vortex. *J. Atmos. Sci.,* **36,** 973–981.

——, and ——, 1984: Hydrodynamic instability of small eddies in a tornado vortex. *J. Atmos. Sci.,* **41,** 422–429.

Steffens, J. L., 1988: The effect of vorticity profile shape on the instability of a two-dimensional vortex. *J. Atmos. Sci.,* **45,** 254–259.

Turkington, B., and N. Whitaker, 1996: Statistical equilibrium computations of coherent structures in turbulent shear layers. *SIAM J. Sci. Comput.,* **17,** 1414–1433.

Vladimirov, V. A., and V. F. Tarasov, 1980: Formation of a system of vortex filaments in a rotating liquid. *Izv. Akad. Az. Nauk SSSR, Mekhanika Zhidkosti i Gaza,* **1,** 44–51.

Wakimoto, R. M., and P. G. Black, 1994: Damage survey of hurricane Andrew and its relationship to the eyewall. *Bull. Amer. Meteor. Soc.,* **75,** 189–200.

Whitaker, N., and B. Turkington, 1994: Maximum entropy states for rotating vortex patches. *Phys. Fluids,* **6,** 3963–3973.

Willoughby, H. E., 1978: A possible mechanism for the formation of hurricane rainbands. *J. Atmos. Sci.,* **35,** 838–848.

——, and P. G. Black, 1996: Hurricane Andrew in Florida: Dynamics of a disaster. *Bull. Amer. Meteor. Soc.,* **77,** 543–549.

——, J. A. Clos, and M. G. Shoreibah, 1982: Concentric eyewalls, secondary wind maxima, and the evolution of the hurricane vortex. *J. Atmos. Sci.,* **39,** 395–411.

Zabusky, N. J., and E. A. Overman, 1983: Regularization of contour dynamical algorithms. *J. Comput. Phys.,* **52,** 351–373.

——, M. H. Hughes, and K. V. Roberts, 1979: Contour dynamics for the Euler equations in two dimensions. *J. Comput. Phys.,* **30,** 96–106.